LJMU Research Online

Tröster, T, Camera, S, Fornasa, M, Regis, M, van Waerbeke, L, Harnois-Déraps, J, Ando, S, Bilicki, M, Erben, T, Fornengo, N, Heymans, C, Hildebrandt, H, Hoekstra, H, Kuijken, K and Viola, M

 Cross-correlation of weak lensing and gamma rays: implications for the nature of dark matter

http://researchonline.ljmu.ac.uk/id/eprint/13354/

Article

Cross-correlation of weak lensing and gamma rays: implications for the nature of dark matter

Tilman Tröster,[1]★ Stefano Camera,[2] Mattia Fornasa,[3] Marco Regis,[4,5]
Ludovic van Waerbeke,[1] Joachim Harnois-Déraps,[6] Shin'ichiro Ando,[3]
Maciej Bilicki,[7] Thomas Erben,[8] Nicolao Fornengo,[4,5] Catherine Heymans,[6]
Hendrik Hildebrandt,[8] Henk Hoekstra,[7] Konrad Kuijken[7] and Massimo Viola[7]

[1]*Department of Physics and Astronomy, The University of British Columbia, 6224 Agricultural Road, Vancouver, B.C., V6T 1Z1, Canada*
[2]*Jodrell Bank Centre for Astrophysics, The University of Manchester, Alan Turing Building, Oxford Road, Manchester M13 9PL, UK*
[3]*Gravitation Astroparticle Physics Amsterdam (GRAPPA), University of Amsterdam, Science Park 904, NL-1098 XH Amsterdam, the Netherlands*
[4]*Dipartimento di Fisica, Università di Torino, via P. Giuria 1, I-10125 Torino, Italy*
[5]*Istituto Nazionale di Fisica Nucleare, Sezione di Torino, via P. Giuria 1, I-10125 Torino, Italy*
[6]*Institute for Astronomy, University of Edinburgh, Royal Observatory, Blackford Hill, Edinburgh EH9 3HJ, UK*
[7]*Leiden Observatory, Leiden University, PO Box 9513, NL-2300 RA Leiden, the Netherlands*
[8]*Argelander-Institut für Astronomie, Auf dem Hügel 71, D-53121 Bonn, Germany*

ABSTRACT
We measure the cross-correlation between *Fermi* gamma-ray photons and over 1000 deg^2 of weak lensing data from the Canada–France–Hawaii Telescope Lensing Survey (CFHTLenS), the Red Cluster Sequence Lensing Survey (RCSLenS), and the Kilo Degree Survey (KiDS). We present the first measurement of tomographic weak lensing cross-correlations and the first application of spectral binning to cross-correlations between gamma rays and weak lensing. The measurements are performed using an angular power spectrum estimator while the covariance is estimated using an analytical prescription. We verify the accuracy of our covariance estimate by comparing it to two internal covariance estimators. Based on the non-detection of a cross-correlation signal, we derive constraints on weakly interacting massive particle (WIMP) dark matter. We compute exclusion limits on the dark matter annihilation cross-section $\langle\sigma_{\rm ann}v\rangle$, decay rate $\Gamma_{\rm dec}$ and particle mass $m_{\rm DM}$. We find that in the absence of a cross-correlation signal, tomography does not significantly improve the constraining power of the analysis. Assuming a strong contribution to the gamma-ray flux due to small-scale clustering of dark matter and accounting for known astrophysical sources of gamma rays, we exclude the thermal relic cross-section for particle masses of $m_{\rm DM} \lesssim 20$ GeV.

Key words: gravitational lensing: weak – dark matter – gamma-rays: diffuse background.

1 INTRODUCTION

The matter content of the Universe is dominated by so-called dark matter whose cosmological abundance and large-scale clustering properties have been measured to high precision (e.g. Hinshaw et al. 2013; Anderson et al. 2014; Hoekstra et al. 2015; Mantz et al. 2015; Ross et al. 2015; Hildebrandt et al. 2017; Planck Collaboration XIII 2016). However, little is known about its microscopic nature, beyond its lack of – or at most weak – non-gravitational interaction with standard model matter.

Weakly interacting massive particles (WIMPs) thermally produced in the early Universe are among the leading dark matter candidates. With a mass of the order of GeV/TeV, their decoupling from thermal equilibrium occurs in the non-relativistic regime. The weak interaction rate with lighter standard model particles furthermore ensures that their thermal relic density is naturally of the order of the measured cosmological dark matter abundance (Lee & Weinberg 1977; Gunn et al. 1978).

Many extensions of the standard model of particle physics predict the existence of new massive particles at the weak scale; some of these extra states can indeed be 'dark', i.e. be colour and electromagnetic neutral, with the weak force and gravity as the only relevant coupling to ordinary matter (for reviews, see e.g. Jungman, Kamionkowski & Griest 1996; Bertone,

★ E-mail: troester@phas.ubc.ca

Hooper & Silk 2005; Schmaltz & Tucker-Smith 2005; Hooper & Profumo 2007; Feng 2010).

The weak coupling allows us to test the hypothesis of WIMP dark matter: supposing that WIMPs are indeed the building blocks of large-scale structure (LSS) in the Universe, there is a small but finite probability that WIMPs in dark matter haloes annihilate or decay into detectable particles. These standard model particles produced by these annihilations or decays would manifest as cosmic rays which can be observed. In particular, since the WIMP mass is around the electroweak scale, gamma rays can be produced, which can be observed with ground-based or space-borne telescopes, e.g. the *Fermi* telescope (Atwood et al. 2009). Indeed, analyses of the gamma-ray sky have already been widely used to put constraints on WIMP dark matter [see e.g. Charles et al. (2016) for a recent review].

The currently strongest constraints on the annihilation cross-section and WIMP mass come from the analysis of local regions with high dark matter content, such as dwarf spheroidal galaxies (dSphs) (Ackermann et al. 2015b). These analyses exclude annihilation cross-sections larger than $\sim 3 \times 10^{-26}\,\mathrm{cm^3\,s^{-1}}$ for dark matter candidates lighter than 100 GeV. This value for the annihilation cross-section is known as the thermal cross-section and, below it, many models of new physics predict dark matter candidates that yield a relic dark matter density in agreement with cosmological measurements of the dark matter abundance (Jungman et al. 1996).

Instead of these local probes of dark matter properties, one could consider the unresolved gamma-ray background (UGRB), i.e. the cumulative radiation produced by all sources that are not bright enough to be resolved individually. Correctly modelling the contribution of astrophysical sources, such as blazars, star-forming and radio galaxies, allows the measurement of the UGRB to be used to constrain the component associated with dark matter (Fornasa & Sánchez-Conde 2015). Indeed, the study of the energy spectrum of the UGRB (Ackermann et al. 2015a), as well as of its anisotropies (Ando & Komatsu 2013; Fornasa et al. 2016) and correlation with tracers of LSS (Ando, Benoit-Lévy & Komatsu 2014; Shirasaki, Horiuchi & Yoshida 2014; Cuoco et al. 2015; Fornengo et al. 2015; Regis et al. 2015; Shirasaki, Horiuchi & Yoshida 2015; Ando & Ishiwata 2016; Feng, Cooray & Keating 2017; Shirasaki et al. 2016) have yielded independent and competitive constraints on the nature of dark matter.

In this paper, we focus on the cross-correlation of the UGRB with weak gravitational lensing. Gravitational lensing is an unbiased tracer of matter and thus closely probes the distribution of dark matter in the Universe. This makes it an ideal probe to cross-correlate with gamma rays to investigate the particle nature of dark matter (Camera et al. 2013).

We extend previous analyses of cross-correlations of gamma rays and weak lensing of Shirasaki et al. (2014, 2016) by adding weak lensing data from the Kilo Degree Survey (KiDS) (de Jong et al. 2013; Kuijken et al. 2015) and making use of the spectral and tomographic information contained within the data sets. This paper presents the first tomographic weak lensing cross-correlation measurement and the first application of spectral binning to the cross-correlation between gamma rays and galaxy lensing. Exploiting tomography and the information contained in the energy spectrum of the dark matter annihilation signal has been shown to greatly increase the constraining power compared to the case where no binning in redshift or energy is performed (Camera et al. 2015).

The structure of this paper is as follows: in Section 2 we introduce the formalism and theory; the data sets are described in Section 3; Section 4 introduces the measurement methods and estimators; the

results are presented in Section 5; and we draw our conclusions in Section 6.

2 FORMALISM

Our theoretical predictions are obtained by computing the angular cross-power spectrum $C_\ell^{g\kappa}$ between the lensing convergence κ and gamma-ray emissions for different classes of gamma-ray sources, denoted by g. In the Limber approximation (Limber 1953), it takes the form

$$C_\ell^{g\kappa} = \int_{\Delta E} \mathrm{d}E \int_0^\infty \mathrm{d}z\, \frac{c}{H(z)} \frac{1}{\chi(z)^2}$$
$$\times\, W_g(E, z)\, W_\kappa(z)\, P_{g\delta}\left(k = \frac{\ell}{\chi(z)}, z\right), \tag{1}$$

where z is the redshift, E is the gamma-ray energy and ΔE the energy bin that is being integrated over, c is the speed of light in the vacuum, $H(z)$ is the Hubble rate, and $\chi(z)$ is the comoving distance. We employ a flat ΛCDM cosmological model with parameters taken from Planck Collaboration XIII (2016).

W_g and W_κ are the window functions that characterize the redshift and energy dependence of the gamma-ray emitters and the efficiency of gravitational lensing, respectively. $P_{g\delta}(k, z)$ is the three-dimensional cross-power spectrum between the gamma-ray emission for a gamma-ray source class and the matter density δ, with k being the modulus of the wavenumber and ℓ the angular multipole. The functional form of the window functions and power spectra depend on the populations of gamma-ray emitters and source galaxy distributions under consideration and are described in the following subsections.

The quantity measured from the data is the tangential shear cross-correlation function $\xi^{g\gamma_t}(\vartheta)$. This correlation function is related to the angular cross-power spectrum by a Hankel transformation:

$$\xi^{g\gamma_t}(\vartheta) = \frac{1}{2\pi} \int_0^\infty \mathrm{d}\ell\, \ell J_2(\ell\vartheta) C_\ell^{g\kappa}, \tag{2}$$

where ϑ is the angular separation in the sky and J_2 is the Bessel function of the first kind of the order of 2.
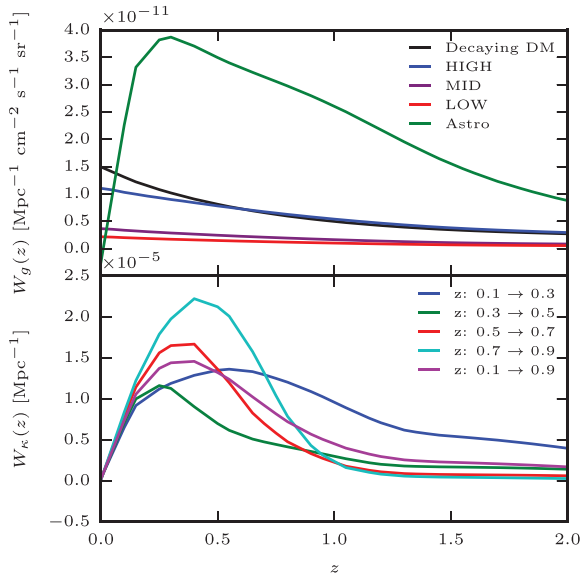
2.1 Window functions

The window function describes the distribution of the signal along the line of sight, averaged over all lines of sight.

2.1.1 Gravitational lensing

For the gravitational lensing the window function is given by (see, e.g. Bartelmann 2010)

$$W_\kappa(z) = \frac{3}{2} H_0^2 \Omega_\mathrm{M}(1+z)\chi(z) \int_z^\infty \mathrm{d}z'\, \frac{\chi(z') - \chi(z)}{\chi(z')} n(z'), \tag{3}$$

where H_0 is the Hubble rate today, Ω_M is the current matter abundance in the Universe, and $n(z)$ is the redshift distribution of background galaxies in the lensing data set. The galaxy distribution depends on the data set and redshift selection, as described in Section 3.1. The redshift distribution function $n(z)$ is binned in redshift bins of width $\Delta_z = 0.05$. To compute the window function in equation (3), $n(z)$ is interpolated linearly between those bins. The resulting window functions for KiDS are shown in the bottom panel of Fig. 1. The width of the window function in Fig. 1, especially for the 0.1–0.3 redshift bin, is due to the leakage of the photometric redshift distribution outside of the redshift selection range.

Figure 1. Top: window functions for the gamma-ray emissions W_g for the energy range 0.5–500 GeV and redshift selection of 0.1–0.9. Shown are the window functions for the three annihilating dark matter scenarios considered, i.e. HIGH (blue), MID (purple), LOW (red); decaying dark matter (black); and the sum of the astrophysical sources (green). The annihilation scenarios assume $m_{DM} = 100$ GeV and $\langle \sigma_{ann} v \rangle = 3 \times 10^{-26}$ cm^3 s^{-1}. For decaying dark matter, $m_{DM} = 200$ GeV and $\Gamma_{dec} = 5 \times 10^{-28}$ s^{-1}. The predictions for annihilating and decaying dark matter are for the $b\bar{b}$ channel. We consider three populations of astrophysical sources that contribute to the UGRB: blazars, mAGNs and SFGs, described in Section 2.1.3. Bottom: the lensing window functions for the five tomographic bins chosen for KiDS.

2.1.2 Gamma-ray emission from dark matter

We consider two processes by which dark matter can create gamma rays: annihilation and decay.

The window function for annihilating dark matter reads (Ando & Komatsu 2006; Fornengo & Regis 2014)

$$W_{g_{ann}}(z, E) = \frac{(\Omega_{DM}\rho_c)^2}{4\pi} \frac{\langle \sigma_{ann} v \rangle}{2m_{DM}^2} (1+z)^3 \Delta^2(z)$$
$$\times \frac{dN_{ann}}{dE} [E(1+z)] e^{-\tau[z, E(1+z)]}, \quad (4)$$

where Ω_{DM} is the cosmological abundance of dark matter, ρ_c is the current critical density of the Universe, m_{DM} is the rest mass of the dark matter particle, and $\langle \sigma_{ann} v \rangle$ denotes the velocity-averaged annihilation cross-section, assumed here to be the same in all haloes. dN_{ann}/dE indicates the number of photons produced per annihilation as a function of photon energy, and sets the gamma-ray energy spectrum. We will consider it to be given by the sum of two contributions: prompt gamma-ray production from dark matter annihilation, which provides the bulk of the emission at low masses, and inverse Compton scattering of highly energetic dark matter-produced electrons and positrons on CMB photons, which upscatter in the gamma-ray band. The final states of dark matter annihilation are computed by means of the PYTHIA Monte Carlo package v8.160 (Sjöstrand, Mrenna & Skands 2008). The inverse Compton scattering contribution is calculated as in Fornasa et al. (2013), which assumes negligible magnetic field and no spatial diffusion for the produced electrons and positrons. Results will be shown for three final states of the annihilation: $b\bar{b}$ pairs, which yields a relatively soft spectrum of photons and electrons, mostly

associated with hadronization into pions and their subsequent decay; $\mu^+\mu^-$, which provides a relatively hard spectrum, mostly associated with final state radiation of photons and direct decay of the muons into electrons; and $\tau^+\tau^-$, which is in between the first two cases, being a leptonic final state but with semi-hadronic decay into pions (Fornengo, Pieri & Scopel 2004; Cembranos et al. 2011; Cirelli et al. 2011).

The optical depth τ in equation (4) accounts for attenuation of gamma rays due to scattering off the extragalactic background light (EBL), and is taken from Franceschini, Rodighiero & Vaccari (2008).

The clumping factor Δ^2 is related to how dark matter density is clustered in haloes and subhaloes. Its definition depends on the square of the dark matter density; therefore, it is a measure of the amount of annihilations happening and, thus, the expected gamma-ray flux. The clumping factor is defined as (see, e.g. Fornengo & Regis 2014)

$$\Delta^2(z) \equiv \frac{\langle \rho_{DM}^2 \rangle}{\bar{\rho}_{DM}^2} = \int_{M_{min}}^{M_{max}} dM \frac{dn_h}{dM}(M, z) [1 + b_{sub}(M, z)]$$
$$\times \int d^3x \frac{\rho_h^2(x|M, z)}{\bar{\rho}_{DM}^2}, \quad (5)$$

where $\bar{\rho}_{DM}$ is the current mean dark matter density, dn_h/dM is the halo mass function (Sheth & Tormen 1999), M_{min} is the minimal halo mass (taken to be 10^{-6} M$_\odot$), M_{max} is the maximal mass of haloes (for definiteness, we use 10^{18} M$_\odot$, but the results are insensitive to the precise value assumed), $\rho_h(x|M, z)$ is the dark matter density profile of a halo with mass M at redshift z, taken to follow a Navarro–Frenk–White (NFW) profile (Navarro, Frenk & White 1997), and b_{sub} is the boost factor that encodes the 'boost' to the halo emission provided by subhaloes. To characterize the halo profile and the subhalo contribution, we need to specify their mass concentration. Modelling the concentration parameter $c(M, z)$ at such small masses and for subhaloes is an ongoing topic of research and is the largest source of uncertainty of the models in this analysis. We consider three cases: LOW, which uses the concentration parameter derived in Prada et al. (2012) (see also Sánchez-Conde & Prada 2014); HIGH, based on Gao et al. (2012); and MID, following the recent analysis of Moliné et al. (2017). The last one represents our reference case with predictions that are normally intermediate between those of the LOW and HIGH. The authors in Moliné et al. (2017) refined the estimation of the boost factor of Sánchez-Conde & Prada (2014) by modelling the dependence of the concentration of the subhaloes on their position in the host halo. Accounting for this dependence and related effects, such as tidal stripping, leads to an increase of a factor of ∼1.7 in the overall boost factor over the LOW model. Predictions for the dark matter clumping factor for the three models are shown in Fig. 2.

Since the number of subhaloes and, therefore, the boost factor increases with increasing host halo mass, the integral in equation (5) is the dominated group and cluster-sized haloes (Ando & Komatsu 2013). However, in the absence of subhaloes, the clumping factor in equation (5) would strongly depend on the low-mass cutoff M_{min}. The minimum halo mass M_{min} depends on the free-streaming scale of dark matter, which is assumed to be in the range of 10^{-12}–10^{-3} M$_\odot$ (Profumo, Sigurdson & Kamionkowski 2006; Bringmann 2009). We therefore choose an intermediary-mass cut-off of $M_{min} = 10^{-6}$ M$_\odot$. As all our models include substructure, the dependence on M_{min} is at most $\mathcal{O}(1)$ (see e.g. fig. S3 in Regis et al. 2015).
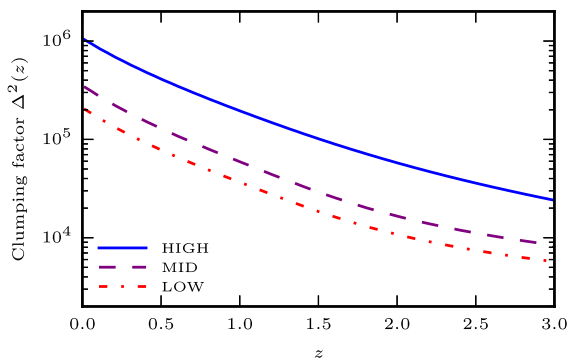
Figure 2. Dark matter clumping factor Δ^2, as defined in equation (5), as a function of redshift for the LOW (dash–dotted red), MID (dashed purple) and HIGH (solid blue) scenarios. The MID model is built from its expression at $z = 0$ in Moliné et al. (2017), assuming the same redshift scaling as in Prada et al. (2012).
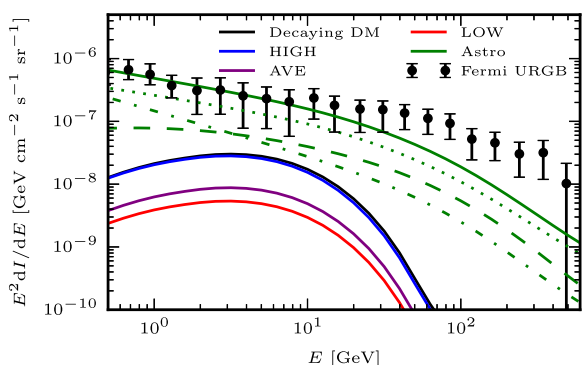
Figure 3. Intensities of the gamma-ray source classes considered in this work: annihilating dark matter assuming HIGH (solid blue), MID (solid purple), LOW (solid red) clustering models; decaying dark matter (solid black); and astrophysical sources (solid green). The dark matter particle properties are the same as in Fig. 1. The astrophysical sources are further divided into blazars (dashed green), mAGN (dotted green) and SFG (dash–dotted green). The black data points represent the observed isotropic component of the UGRB (Ackermann et al. 2015c).

The window function of decaying dark matter is given by (Ando & Komatsu 2006; Ibarra, Tran & Weniger 2013; Fornengo & Regis 2014)

$$W_{g_{\text{dec}}}(z, E) = \frac{\Omega_{\text{DM}} \rho_c}{4\pi} \frac{\Gamma_{\text{dec}}}{m_{\text{DM}}} \frac{dN_{\text{dec}}}{dE} [E(1+z)] \, e^{-\tau[z, E(1+z)]}, \quad (6)$$

where Γ_{dec} is the decay rate and $\frac{dN_{\text{dec}}}{dE}(E) = \frac{dN_{\text{ann}}}{dE}(2E)$, i.e. the energy spectrum for decaying dark matter, is the same as that for annihilating dark matter described above, at twice the energy (Cirelli et al. 2011). Unlike annihilating dark matter, decaying dark matter does not depend on the clumping factor and the expected emission is thus much less uncertain. A set of representative window functions for annihilating and decaying dark matter is shown in the top panel of Fig. 1. In Fig. 3 we show the average all-sky gamma-ray emission expected from annihilating dark matter for the three clumping scenarios described above and from decaying dark matter.

2.1.3 Gamma-ray emission from astrophysical sources

Besides dark matter, gamma rays are produced by astrophysical sources which will contaminate, and even dominate over the

expected dark matter signal. Indeed, astrophysical sources have been shown to be able to fully explain the observed cross-correlations between gamma rays and tracers of LSS, like galaxy catalogues (Cuoco et al. 2015; Xia et al. 2015). For this analysis, we model three populations of astrophysical sources of gamma rays: blazars, misaligned active galactic nuclei (mAGNs) and star-forming galaxies (SFGs). The sum of the gamma-ray emissions produced by the three extragalactic astrophysical populations described above approximately accounts for all the UGRB measured (see Fornasa & Sánchez-Conde 2015), as shown Fig. 3, where the emissions from the three astrophysical source classes are compared to the most recent measurement of the UGRB energy spectrum from Ackermann et al. (2015c). For each of these astrophysical gamma-ray sources, we consider a window function of the form

$$W_{g_S}(z, E) = \chi(z)^2 \int_{\mathcal{L}_{\text{min}}}^{\mathcal{L}_{\text{max}}(F_{\text{sens}}, z)} d\mathcal{L} \frac{dF}{dE}(\mathcal{L}, z) \, \Phi(\mathcal{L}, z), \quad (7)$$

where $\mathcal{L}$ is the gamma-ray luminosity in the energy interval 0.1–100 GeV, and Φ is the gamma-ray luminosity function (GLF) corresponding to one of the source classes of astrophysical emitters included in our analysis. The upper bound, $\mathcal{L}_{\text{max}}(F_{\text{sens}}, z)$, is the luminosity above which an object can be resolved, given the detector sensitivity F_{sens}, taken from Ackermann et al. (2015d). As we are interested in the contribution from unresolved astrophysical sources, only sources with luminosities smaller than $\mathcal{L}_{\text{max}}$ are included. Conversely, the minimum luminosity $\mathcal{L}_{\text{min}}$ depends on the properties of the source class under investigation. The differential photon flux is given by $dF/dE = dN_S/dE \times e^{-\tau[z, E(1+z)]}$, where dN_S/dE is the observed energy spectrum of the specific source class and the exponential factor again accounts for the attenuation of high-energy photons by the EBL.

We consider a unified blazar model combining BL Lacertae and flat-spectrum radio quasars as a single source class. The GLF and energy spectrum are taken from Ajello et al. (2015) where they are derived from a fit to the properties of resolved blazars in the third *Fermi*-LAT catalogue (Acero et al. 2015).

In the case of mAGN, we follow Di Mauro et al. (2014), who studied the correlation between the gamma-ray and radio luminosity of mAGN, and derived the GLF from the radio luminosity function. We consider their best-fitting $\mathcal{L}$–$L_{r,\text{core}}$ relation and assume a power-law spectrum with index $\alpha_{\text{mAGN}} = 2.37$.

To build the GLF of SFG, we start from the IR luminosity function of Gruppioni et al. (2013) (adding up spiral, starburst and SF-AGN populations of their table 8) and adopt the best-fitting $\mathcal{L}$–L_{IR} relation from Ackermann et al. (2012). The energy spectrum is taken to be a power law with spectral index $\alpha_{\text{SFG}} = 2.7$.

The window function and average all-sky emission expected from the astrophysical sources are shown as green lines in the top panel of Figs 1 and 3, respectively.

2.2 Three-dimensional power spectrum

The three-dimensional cross-power spectrum $P_{g\delta}$ between the gamma-ray emission of a source class g and the matter density is defined as

$$\langle \hat{f}_g(z, \boldsymbol{k}) \hat{f}_\delta^*(z', \boldsymbol{k}') \rangle = (2\pi)^3 \delta^3(\boldsymbol{k} + \boldsymbol{k}') P_{g\delta}(k, z, z'), \quad (8)$$

where $\hat{f}_g$ and $\hat{f}_\delta$ denote the Fourier transform of the emission of the specific class of gamma-ray emitters and matter density, respectively, and $\langle . \rangle$ indicates the average over the survey volume. Using the Limber approximation, one can set $z = z'$ in equation (8). The

density of gamma-ray emission due to decaying dark matter traces the dark matter density contrast $\delta_{\rm DM}$, while the emission associated with annihilating dark matter traces $\delta_{\rm DM}^2$. Astrophysical sources are assumed to be point-like biased tracers of the matter distribution. Finally, lensing directly probes the matter contrast $\delta_{\rm M}$. To compute $P_{g\delta}$, we follow the halo model formalism (for a review, see e.g. Cooray & Sheth 2002), and write $P = P^{\rm 1h} + P^{\rm 2h}$. We derive the one-halo term $P^{\rm 1h}$ and the two-halo term $P^{\rm 2h}$ as in Fornengo et al. (2015) and in Camera et al. (2015).

2.2.1 Dark matter gamma-ray sources

The 3D cross-power spectrum between dark matter sources of gamma rays and matter density is given by:

$$P^{\rm 1h}_{g_{\rm DM}\kappa}(k,z) = \int_{M_{\rm min}}^{M_{\rm max}} {\rm d}M \, \frac{{\rm d}n_{\rm h}}{{\rm d}M}(M,z) \, \hat{v}_{g_{\rm DM}}(k|M,z) \, \hat{u}_\kappa(k|M,z)$$

$$\begin{aligned}
P^{\rm 2h}_{g_{\rm DM}\kappa}(k,z) = {} & \left[\int_{M_{\rm min}}^{M_{\rm max}} {\rm d}M \, \frac{{\rm d}n_{\rm h}}{{\rm d}M}(M,z) \, b_{\rm h}(M,z) \, \hat{v}_{g_{\rm DM}}(k|M,z) \right] \\
& \times \left[\int_{M_{\rm min}}^{M_{\rm max}} {\rm d}M \, \frac{{\rm d}n_{\rm h}}{{\rm d}M}(M,z) \, b_{\rm h}(M,z) \hat{u}_\kappa(k|M,z) \right] \\
& \times P^{\rm lin}(k,z),
\end{aligned} \tag{9}$$

where $P^{\rm lin}$ is the linear matter power spectrum, $b_{\rm h}$ is the linear bias (taken from the model of Sheth & Tormen 1999) and $\hat{u}_\kappa(k|M,z)$ is the Fourier transform of the matter halo density profile, i.e. $\rho_{\rm h}(\boldsymbol{x}|M,z)/\bar{\rho}_{DM}$. The Fourier transform of the gamma-ray emission profile for dark matter haloes is described by $\hat{v}_{g_{\rm DM}}(k|M,z)$. For decaying dark matter, $\hat{v}_{g_{\rm DM}} = \hat{u}_\kappa$, i.e. the emission follows the dark matter density profile. Conversely, the emission for annihilating dark matter follows the square of the dark matter density profile: $\hat{v}_{g_{\rm DM}}(k|M,z) = \hat{u}_{\rm ann}(k|M,z)/\Delta(z)^2$, where $\hat{u}_{\rm ann}$ is the Fourier transform of the square of the main halo density profile plus its substructure contribution, and $\Delta(z)^2$ is the clumping factor. The mass limits are $M_{\rm min} = 10^{-6} \, {\rm M}_\odot$ and $M_{\rm max} = 10^{18} \, {\rm M}_\odot$ again.

2.2.2 Astrophysical gamma-ray sources

The cross-correlation of the convergence with astrophysical sources is sourced by the 3D power spectrum

$$P^{\rm 1h}_{g_{\rm S}\kappa}(k,z) = \int_{\mathcal{L}_{\rm min}}^{\mathcal{L}_{\rm max}} {\rm d}\mathcal{L} \, \frac{\Phi(\mathcal{L},z)}{\langle f_{\rm S} \rangle} \frac{{\rm d}F}{{\rm d}E}(\mathcal{L},z) \, \hat{u}_\kappa(k|M(\mathcal{L},z),z)$$

$$\begin{aligned}
P^{\rm 2h}_{g_{\rm S}\kappa}(k,z) = {} & \left[\int_{\mathcal{L}_{\rm min}}^{\mathcal{L}_{\rm max}} {\rm d}\mathcal{L} \, b_{\rm S}(\mathcal{L},z) \, \frac{\Phi_i(\mathcal{L},z)}{\langle f_{\rm S} \rangle} \frac{{\rm d}F}{{\rm d}E}(\mathcal{L},z) \right] \\
& \times \left[\int_{M_{\rm min}}^{M_{\rm max}} {\rm d}M \, \frac{{\rm d}n_{\rm h}}{{\rm d}M}(M,z) \, b_{\rm h}(M,z) \hat{u}_\kappa(k|M,z) \right] \\
& \times P^{\rm lin}(k,z),
\end{aligned} \tag{10}$$

where $b_{\rm S}$ is the bias of gamma-ray astrophysical sources with respect to the matter density, for which we adopt $b_{\rm S}(\mathcal{L},z) = b_{\rm h}(M(\mathcal{L},z))$. That is, a source with luminosity $\mathcal{L}$ has the same bias $b_{\rm h}$ as a halo with mass M, with the relation $M(\mathcal{L},z)$ between the mass of the host halo M and the luminosity of the hosted object $\mathcal{L}$ taken from Camera et al. (2015). The mean flux $\langle f_{\rm S} \rangle$ is defined as $\langle f_{\rm S} \rangle = \int {\rm d}\mathcal{L} \frac{{\rm d}F}{{\rm d}E} \Phi$.

3 DATA

3.1 Weak lensing data sets

For this study we combine CFHTLenS[1] and RCSLenS[2] data sets from the Canada–France–Hawaii Telescope (CFHT) and KiDS[3] from the VLT Survey Telescope (VST), all of which have been optimized for weak lensing analyses. The same photometric redshift and shape measurement algorithms have been used in the analysis of the three surveys. However, there are slight differences in the algorithm implementation and in the shear and photometric redshift calibration, as described in the following subsections.

The sensitivity of the measurement depends inversely on the overlap area between the gamma-ray map and the lensing data, with a weaker dependence on the parameters characterizing the lensing sensitivity, i.e. the galaxy number density and ellipticity dispersion. This is due to the fact that at large scales, sampling variance dominates the contribution of lensing to the covariance and reducing the shape noise does not result in an improvement of the overall covariance. This point is further discussed in Section 4.2.1.

Of the three surveys, only CFHTLenS and KiDS have full photometric redshift coverage. We choose to restrict the tomographic analysis to KiDS, as the much smaller area of CFHTLenS is expected to yield a much lower sensitivity for this measurement. In Section 5.2 we find that tomography does not appreciably improve the exclusion limits on the dark matter parameters. We thus do not lose sensitivity by restricting the tomographic analysis to KiDS in this work.

3.1.1 CFHTLenS

CFHTLenS spans a total area of 154 deg^2 from a mosaic of 171 individual MEGACAM pointings, divided into four compact regions (Heymans et al. 2012). Details on the data reduction are described in Erben et al. (2013). The observations in the five bands *ugriz* of the survey allow for the precise measurement of photometric redshifts (Hildebrandt et al. 2012). The shape measurement with LENSFIT is described in detail in Miller et al. (2013). We make use of all fields in the data set as we are not affected by the systematics that lead to field rejections in the cosmic shear analyses (Kilbinger et al. 2013). We correct for the additive shear bias for each galaxy individually, while the multiplicative bias is accounted for on an ensemble basis, as described in Section 4.1.

Individual galaxies are selected based on the Bayesian photometric redshift $z_{\rm B}$ being in the range [0.2, 1.1]. The resulting redshift distribution of the selected galaxies is obtained by stacking the redshift probability distribution function of individual galaxies, weighted by the LENSFIT weight. As a result of the stacking of the individual redshift PDFs, the true redshift distribution leaks outside the $z_{\rm B}$ selection range. Stacking the redshift PDFs can lead to biased estimates of the true redshift distribution of the source galaxies (Choi et al. 2016) but in light of the large statistical and modelling uncertainties in this analysis these biases can be safely neglected here.

---

[1] http://www.cfhtlens.org/
[2] http://www.rcslens.org/
[3] http://kids.strw.leidenuniv.nl/

3.1.2 RCSLenS

The RCSLenS data consist of 14 disconnected regions whose combined total area reaches 785 deg^2. A full survey and lensing analysis description is given in Hildebrandt et al. (2016). RCSLenS uses the same LENSFIT version as CFHTLenS but with a different size prior, as galaxy shapes are measured from *i*-band images in CFHTLenS, whereas RCSLenS uses the *r* band. The additive and multiplicative shear biases are accounted for in the same fashion as in CFHTLenS.

Multi-band photometric information is not available for the whole RCSLenS footprint, therefore we use the redshift distribution estimation technique described in Harnois-Déraps et al. (2016) and Hojjati et al. (2016). Of the three magnitude cuts considered in Hojjati et al. (2016), we choose to select the source galaxies such that $18 < \mathrm{mag_r} < 26$, as this selection yielded the strongest cross-correlation signal in Hojjati et al. (2016). This cut is close to the $18 < \mathrm{mag_r} < 24$ in Harnois-Déraps et al. (2016) but with the faint cutoff determined by the shape measurement algorithm. The redshift distribution is derived from the CFHTLenS-VIPERS sample (Coupon et al. 2015), a UV and IR extension of CFHTLenS. We stack the redshift PDF in the CFHTLenS-VIPERS sample, accounting for the RCSLenS magnitude selection, *r*-band completeness and galaxy shape measurement (LENSFIT) weights.

3.1.3 KiDS

The third data set considered here comes from the KiDS, which currently covers 450 deg^2 with complete *ugri* four band photometry in five patches. Galaxy shapes are measured in the *r* band using the new self-calibrating LENSFIT (Fenech Conti et al. 2016). Cross-correlation studies such as this work are only weakly sensitive to additive biases and, being linear in the shear, are less affected by multiplicative biases than cosmic shear studies. Nonetheless, the analysis still benefits from well-calibrated shape measurements. The residual multiplicative shear bias is accounted for on an ensemble basis, as for CFHTLenS and RCSLenS. To correct for the additive bias we subtract the LENSFIT weighted ellipticity means in each tomographic bin. A full description of the survey and data products is given in Hildebrandt et al. (2017).

We select galaxies with $0.1 \leq z_\mathrm{B} < 0.9$ and then further split the data into four tomographic bins [0.1, 0.3], [0.3, 0.5], [0.5, 0.7] and [0.7, 0.9]. We derive the effective $n(z)$ following the DIR method introduced in Hildebrandt et al. (2017).

3.2 *Fermi*-LAT

For this work we use *Fermi* data gathered until 2016 September 1, spanning over eight years of observations. We use Pass 8 event reconstruction and reduce the data using FERMI SCIENCE TOOLS version v10r0p5. We select FRONT+BACK converting events (evtype=3) between energies of 0.5 and 500 GeV. We restrict our main analysis to ultracleanveto photons (evclass=1024). We verify that selecting clean photons (evclass=256) does not change the results of the analysis. Furthermore, we apply the cuts (DATA_QUAL>0)&&(LAT_CONFIG==1) on the data quality. We then create full sky HEALPIX[4]

---

[4] http://healpix.sourceforge.net/

photon count and exposure maps with nside=1024 (Górski et al. 2005) in 20 logarithmically spaced energy bins in the range mentioned above.

The flux map used in the cross-correlation analysis is obtained by dividing the count maps by the exposure maps in each energy bin before adding them. We have confirmed that the energy spectrum of the individual flux maps follows a broken power law with an index of 2.34 ± 0.02, consistent with that obtained in previous studies of the UGRB (Ackermann et al. 2015a).

We also create maps for four energy bins 0.5–0.766 GeV, 0.766–1.393 GeV, 1.393–3.827 GeV and 3.827–500 GeV. The bins are chosen such that they would contain equal photon counts for a power-law spectrum with index 2.5. The flux maps for the four energy bins are computed by first dividing each energy bin into three logarithmically spaced bins, creating flux maps for these fine bins, and then adding them up.

The total flux is dominated by resolved point sources and, to a lesser extent, by diffuse Galactic emissions. To probe the unresolved component of the gamma-ray sky, we mask the 500 brightest point sources in the third *Fermi* point source catalogue (Acero et al. 2015) with circular masks with a radius of two degrees. The remaining point sources are masked with one degree circular masks. We checked that the analysis is robust with respect to other masking strategies. The effect of the diffuse Galactic emission (DGE) is minimized by subtracting the gll_iem_v06 model. Furthermore, we employ a 20° cut in Galactic latitude. It has been shown in Shirasaki et al. (2016) that this cross-correlation analysis is robust against the choice made for the model of DGE. We have confirmed that our results are not significantly affected even in the extreme scenario of not removing the DGE at all. This represents an important benefit of using cross-correlations to study the UGRB over studies of the energy spectrum alone, as in Ackermann et al. (2015a).

The robustness of these selection and cleaning choices is demonstrated in Fig. A3, where the impact of the event selection, point source masks and cleaning of the DGE on the cross-correlation signal is shown. None of these choices leads to a significant change in the measured correlation signal, highlighting the attractive feature of cross-correlation analyses that uncorrelated quantities, such as Galactic emissions and extragalactic effects like lensing, do not bias the signal.

The point spread function (PSF) of *Fermi* is energy dependent and, especially at low energies, significantly reduces the cross-correlation signal power at small angular scales, as demonstrated in Fig. 4. The pixelation of the gamma-ray sky has a similar but much weaker effect. In this analysis, we choose to account for this suppression of power by forward modelling. That is, rather than correcting the measurements, the predicted angular power spectra $C_\ell^{g\kappa}$ are modified to account for the effect of the PSF and pixel window function.

The gamma-ray data used in the analysis are obtained by cutting out regions around the lensing footprints. To increase the sensitivity at large angular scales, we include an additional four degree wide band around each of the 23 lensing patches.
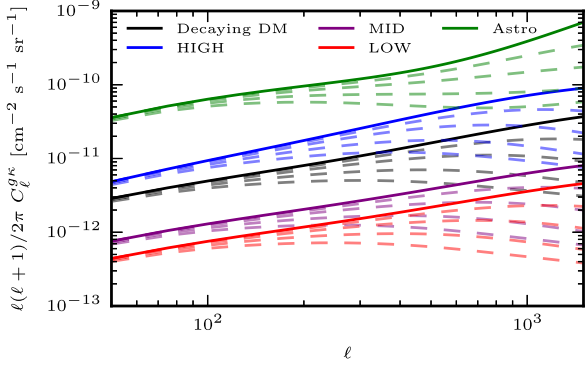
4 METHODS

4.1 Estimators

To measure the cross-correlation function between gamma rays and lensing, we employ the tangential shear estimator (see also Shirasaki

Figure 4. Model $C_\ell^{g\kappa}$ for three annihilating dark matter scenarios, decaying dark matter and astrophysical sources. The models and formatting are the same as in Figs 1 and 3. The models assume the $n(z)$ for the $z \in [0.1, 0.9]$ bin for KiDS and the energy range 0.5–500 GeV. The dashed lines indicate the effect of the *Fermi* PSF on the cross-power spectrum for the four energy bins, with the lowest energy bin having the strongest suppression of power at small scales. For clarity, the effect of the PSF for the different energy bins is shown on the cross-power spectrum $C_\ell^{g\kappa}$ for the single energy bin of 0.5–500 GeV.

et al. 2014; Harnois-Déraps et al. 2016; Hojjati et al. 2016):

$$\hat{\xi}^{g\gamma_{t/x}}(\vartheta) = \frac{\sum_{ij} w_i e_{ij}^{t/x} g_j \Delta_{ij}(\vartheta)}{\sum_{ij} w_i \Delta_{ij}(\vartheta)} \frac{1}{1 + K(\vartheta)},$$

$$\frac{1}{1 + K(\vartheta)} = \frac{\sum_{ij} w_i \Delta_{ij}(\vartheta)}{\sum_{ij} w_i (1 + m_i) \Delta_{ij}(\vartheta)}, \qquad (11)$$

where the sum runs over all galaxies i and pixels j of the gamma-ray flux map, w_i is the LENSFIT-weight of galaxy i and $e_{ij}^{t/x}$ is the tangential (t) or cross (x) component of the shear with respect to the position of pixel j, g_j is the flux at pixel j, and $\Delta_{ij}(\vartheta)$ accounts for the angular binning, being equal to 1 if the distance between galaxy i and pixel j falls within the angular bin centred on ϑ and 0 otherwise. The factor of $\frac{1}{1+K}$ accounts for the multiplicative shear bias, with m_i being the multiplicative shear bias of galaxy i.

The $\hat{\xi}^{g\gamma_{t/x}}(\vartheta)$ measurement described with equation (11) exhibits strong correlation between the angular bins at all scales. This complicates the estimation of the covariance matrix as the off-diagonal elements have to be estimated accurately. On the other hand, the covariance of the angular cross-power spectrum $\hat{C}_\ell^{g\kappa}$ is largely diagonal since the measurement is noise-dominated. We thus choose to work with angular power spectrum $\hat{C}_\ell^{g\kappa}$ instead of the correlation function $\hat{\xi}^{g\gamma_t}(\vartheta)$. Inverting the relation in equation (2), one can construct an estimator for the angular cross-power spectrum $\hat{C}_\ell^{g\kappa}$ based on the measurement of $\hat{\xi}^{g\gamma_t}(\vartheta)$ (Szapudi et al. 2001; Schneider et al. 2002). Specifically, working in the flat-sky approximation, one can write

$$\hat{C}_\ell^{g\kappa} = 2\pi \int_0^\infty d\vartheta \, \vartheta \, J_2(\ell\vartheta) \hat{\xi}^{g\gamma_t}(\vartheta). \qquad (12)$$

This estimator yields an estimate for the cross-power spectrum between the gamma rays and the E mode of the shear field. Replacing the tangential shear γ_t in equation (12) with the cross-component of the shear γ_x results in an estimate of the cross-power spectrum between the gamma rays and the B mode of the shear field, which is expected to vanish in the absence of lensing systematics. In Appendix A, we check that this estimator indeed accurately recovers the underlying power spectrum.

To estimate the power spectrum using estimator in equation (12), we measure the tangential shear between 1 and 301 arcmin in 300

linearly spaced bins. The resulting power spectrum is then binned in five linearly spaced bins between ℓ of 200 and 1500. At smaller scales the *Fermi* PSF suppresses power, especially at low energies. At very large scales of $\ell \lesssim 100$, the covariance is affected by residuals from imperfect foreground subtraction, hence we restrict ourselves to scales of $\ell > 200$.

4.2 Covariances

Our primary method to estimate the covariance relies on a Gaussian analytical prescription. This is justified because the covariance is dominated by photon and shape noise, both of which can be modelled accurately. To verify that this analytical prescription is a good estimate of the true covariance, we compare it to two internal covariance estimators which estimate the covariance from the data. In the first, we select random patches on the gamma-ray flux map and correlate them with the lensing data, as described in Section 4.2.2. For the second method we randomize the pixels of the gamma-ray flux map within the patches used in the cross-correlation measurement, described in Section 4.2.3.

Unlike an analytical covariance, inverting covariances estimated from a finite number of realizations incurs a bias (Kaufman 1967; Hartlap, Simon & Schneider 2007; Taylor, Joachimi & Kitching 2013; Sellentin & Heavens 2016). The bias is dependent on the number of degrees of freedom in the measurement. Combining measurements of multiple energy or redshift bins increases the size of the measurement vector. Specifically, in the case of no binning in redshift or energy, the data vector has five elements, when binning in either redshift or energy, it contains 20 elements, and when binning in both redshift and energy, its length is 80. For a fixed number of realizations, the bias therefore changes depending on which data are used in the analysis, diminishing the advantage gained by combining multiple energy or redshift bins and making comparisons between different binning strategies harder. For this reason, we choose the analytical prescription as our primary method to estimate the covariance.

The diagonal elements of the three covariance estimates are shown in Fig. 5 for the case of KiDS, showing good agreement between all three approaches. The limits derived from the three covariance estimations agree as well. Choosing the analytical prescription as our primary method is thus justified.
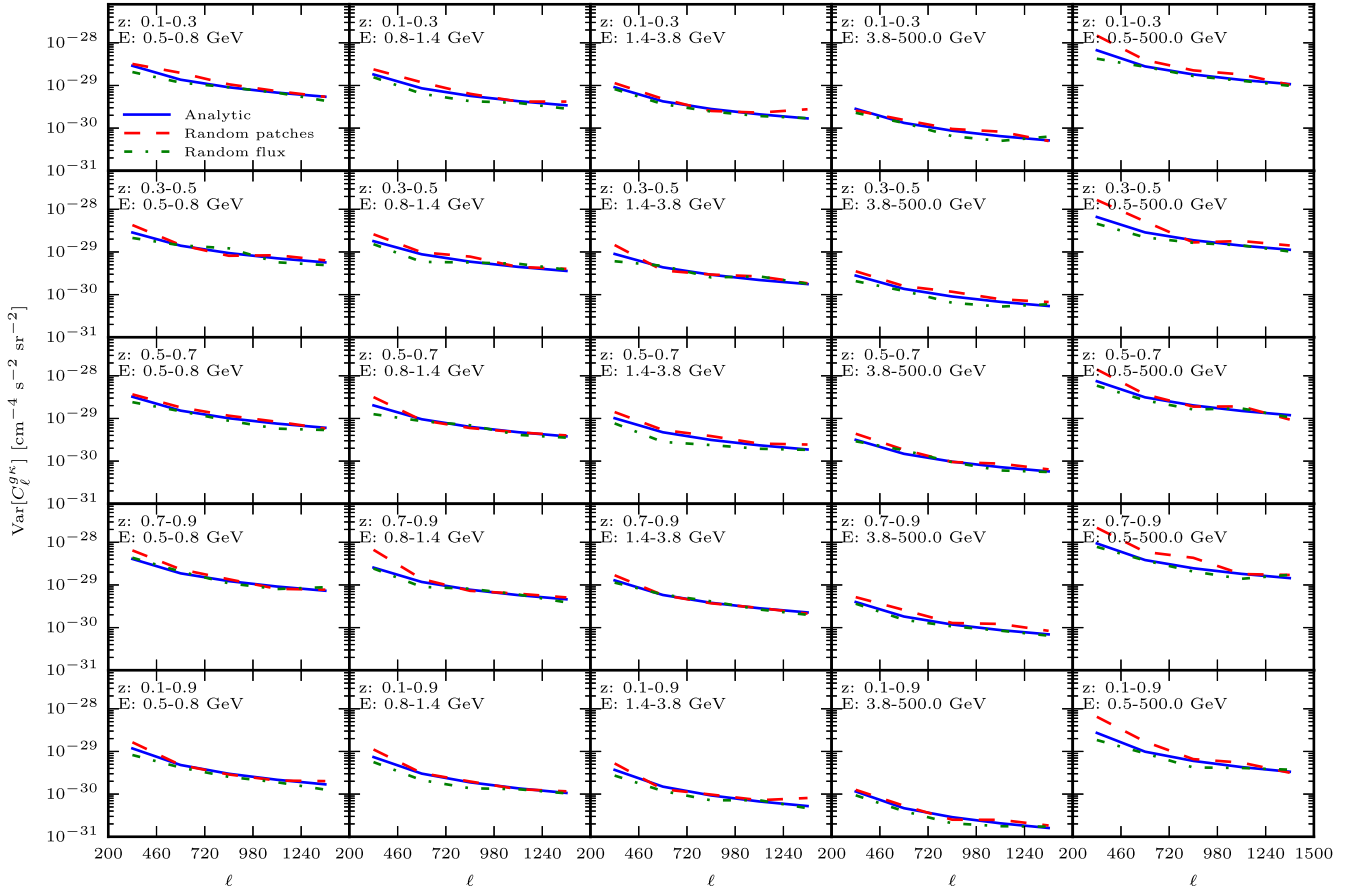
4.2.1 Analytical covariance

We model the covariance **C** as

$$\mathbf{C}[C_\ell^{g\kappa}] = \frac{1}{f_{\rm sky}(2\ell+1)\Delta_\ell} \left(\hat{C}_\ell^{gg} \hat{C}_\ell^{\kappa\kappa} + \left(\hat{C}_\ell^{g\kappa} \right)^2 \right), \qquad (13)$$

where $f_{\rm sky}$ denotes the fraction of the sky that is covered by the effective area of the survey, Δ_ℓ is the ℓ-bin width, $\hat{C}_\ell^{gg}$ is an estimate of the gamma-ray auto-power spectrum, $\hat{C}_\ell^{\kappa\kappa}$ is the convergence auto-power spectrum, and $\hat{C}_\ell^{g\kappa}$ is the cross-spectrum between gamma rays and the convergence, calculated as described in Section 2. The effective area for the cross-correlation is given by the product of the masks of the gamma-ray map and lensing data, which corresponds to 99, 308 and 362 deg^2 for CFHTLenS, RCSLenS and KiDS, respectively.

The gamma-ray auto-power spectrum $\hat{C}_\ell^{gg}$ is estimated from the same gamma-ray flux maps as used in the cross-correlation. We measure the auto-spectra of the five energy bins and the

Figure 5. The diagonal elements of the analytical covariance (solid blue), covariance from random patches (dashed red) and covariance from randomized flux (dot–dashed green) for the five energy and redshift bins for KiDS. All three estimates agree at small scales, while the covariance derived from random patches shows a slight excess of variance at large scales.

cross-spectra between the energy bins using POLSPICE[5] in 15 logarithmically spaced ℓ-bins between ℓ of 30 and 2000. Because the measurement is very noisy at large scales, we fit the measured spectra with a spectrum of the form

$$\hat{C}_\ell^{gg} = C_P + c\,\ell^\alpha, \qquad (14)$$

where C_P is the Poisson noise term, and c and α describe a power-law contribution to account for a possible increase of power at very large scales. The value of the intercept c is consistent with zero in all cases while best-fitting Poisson noise terms are consistent with a direct estimate based on the mean number of photon counts, i.e.

$$C_P = \frac{\langle n_g/\epsilon^2 \rangle}{\Omega_{\rm pix}}, \qquad (15)$$

where n_g is the number of observed photons per pixel, ϵ the exposure per pixel, and $\Omega_{\rm pix}$ the solid angle covered by each pixel (Fornasa et al. 2016). Except for the lowest energies, the observed intrinsic angular auto-power spectrum is sub-dominant to the photon shot noise (Fornasa et al. 2016).

The lensing auto-power spectrum is given by

$$\hat{C}_\ell^{\kappa\kappa} = C_\ell^{\kappa\kappa} + \frac{\sigma_e^2}{n_{\rm eff}}, \qquad (16)$$

Table 1. Total number of galaxies with shape measurements, $n_{\rm gal}$, effective galaxy number density, $n_{\rm eff}$, and ellipticity dispersion σ_e for CFHTLenS, RCSLenS and KiDS for the cuts employed in this analysis. We follow the prescription in Heymans et al. (2012) to calculate $n_{\rm eff}$ and σ_e.

	$n_{\rm gal}$	$n_{\rm eff}$ [arcmin^{-2}]	σ_e
CFHTLenS	47 60 606	9.44	0.279
RCSLenS	144 90 842	5.84	0.277
KiDS $0.1 \leq z_B < 0.3$	37 69 174	2.23	0.290
KiDS $0.3 \leq z_B < 0.5$	32 49 574	2.03	0.282
KiDS $0.5 \leq z_B < 0.7$	29 41 861	1.81	0.273
KiDS $0.7 \leq z_B < 0.9$	26 40 577	1.49	0.276
KiDS $0.1 \leq z_B < 0.9$	126 01 186	7.54	0.281

where $C_\ell^{\kappa\kappa}$ is the cosmic shear signal and $\frac{\sigma_e^2}{n_{\rm eff}}$ is the shape noise term, with σ_e^2 being the dispersion per ellipticity component and $n_{\rm eff}$ the galaxy number density. These parameters are listed in Table 1. The cosmic shear term $C_\ell^{\kappa\kappa}$ is calculated using the halo-model. The two terms in equation (16) are of similar magnitude, with the shape noise dominating at small scales and sampling variance dominating at large scales. Decreasing σ_e or increasing $n_{\rm eff}$ thus only improves the covariance at scales where the shape noise makes a significant contribution to equation (16). However, increasing the area of the lensing survey and thus the overlap with the gamma-ray map directly decreases the covariance inversely proportionally to the overlap area. For this reason CFHTLenS has a low sensitivity

[5] http://www2.iap.fr/users/hivon/software/PolSpice/

in this analysis, even though it is the deepest survey of the three. Although RCSLenS has the largest effective area, the covariance for KiDS is slightly smaller since the increase in depth is large enough to overcome the area advantage of RCSLenS.

4.2.2 Random patches

We select 100 random patches from the gamma-ray map as an approximation of independent realizations of the gamma-ray sky. The patches match the shape of the original gamma-ray cutouts, i.e. the lensing footprints plus a four degree wide band, but have their position and orientation randomized. The patches are chosen such that they do not lie within the Galactic latitude cut.

These random patches are uncorrelated with the lensing data but preserve the auto-correlation of the gamma rays and hence account for sampling variance in the gamma-ray sky, including residuals of the foreground subtraction.

For small patches, the assumption of independence is quite accurate, as the probability of two random patches overlapping is low. Larger patches will correlate to a certain degree. This lack of independence might lead to an underestimation of the covariance. This correlation is minimized by rotating each random patch, making the probability of having two very similar patches low.

The diagonal elements of the resulting covariance are shown in Fig. 5. While the agreement with the Gaussian covariance is good at small scales, there is an excess of variance at large scales for some energy and redshift bins. This excess can be explained by a large-scale modulation of the power in the gamma-ray map, which would be sampled by the random patches. This interpretation is consistent with the strong growth of the error bars of the gamma-ray auto-correlation towards large scales. However, the results of the analysis are not affected significantly by this.

4.2.3 Randomized flux

In a further test of the analytical covariance in equation (13), we randomize the gamma-ray pixel positions within each patch. This preserves the one-point statistics of the flux while destroying any spatial correlations. This approach is similar to the random Poisson realizations used in Shirasaki et al. (2014) but we use the actual one-point distribution of the data itself instead of assuming a Poisson distribution.

Because the pixel values are not correlated anymore, contributions to the large-scale variance due to imperfect foreground subtraction or leakage of flux from point sources outside of their masks are removed.

The covariance derived from 100 such random flux maps is in good agreement with both the analytical covariance and the covariance estimated from random patches, as shown in Fig. 5.

4.3 Statistical methods

The likelihood function we employ to find exclusion limits on the annihilation cross-section $\langle \sigma_{ann} v \rangle$ or decay rate Γ_{dec} and WIMP mass m_{DM} is given by

$$\mathcal{L}(\boldsymbol{\alpha}|\boldsymbol{d}) \propto e^{-\frac{1}{2}\chi^2(\boldsymbol{d},\boldsymbol{\alpha})}, \tag{17}$$

with

$$\chi^2(\boldsymbol{d}, \boldsymbol{\alpha}) = (\boldsymbol{d} - \boldsymbol{\mu}(\boldsymbol{\alpha}))^{\mathrm{T}} \, \mathsf{C}^{-1} \, (\boldsymbol{d} - \boldsymbol{\mu}(\boldsymbol{\alpha})), \tag{18}$$

where $\boldsymbol{d}$ denotes the data vector, $\boldsymbol{\mu}(\boldsymbol{\alpha})$ the model vector, $\boldsymbol{\alpha}$ the parameters considered in the fit, i.e. either the cross-section $\langle \sigma_{ann} v \rangle$ and the particle mass m_{DM} or the decay rate Γ_{dec} and m_{DM}. The amplitude of the cross-correlation signal expected from astrophysical sources is kept fixed and thus does not contribute as an extra free parameter. Finally, C^{-1} is the inverse of the data covariance.

The limits on $\langle \sigma_{ann} v \rangle$ and Γ_{dec} correspond to contours of the likelihood surface described by equation (17). Specifically, for a given confidence interval p, the contours are given by the set of parameters $\boldsymbol{\alpha}_{cont.}$ for which

$$\chi^2(\boldsymbol{d}, \boldsymbol{\alpha}_{cont.}) = \chi^2(\boldsymbol{d}, \boldsymbol{\alpha}_{ML}) + \Delta_{\chi^2}(p), \tag{19}$$

where $\boldsymbol{\alpha}_{ML}$ is the maximum likelihood estimate of the parameters $\langle \sigma_{ann} v \rangle$ or Γ_{dec} and m_{DM}, χ^2 is given by equation (18), and $\Delta_{\chi^2}(p)$ corresponds to the quantile function of the χ^2-distribution. For this analysis we are dealing with two degrees of freedom and require 2σ contours, hence $\Delta_{\chi^2}(0.95) = 6.18$.

This approach to estimate the exclusion limits follows recent studies, such as Shirasaki et al. (2016). It should be noted that deriving the limits on $\langle \sigma_{ann} v \rangle$ or Γ_{dec} for a fixed mass m_{DM} is also common in the literature [see e.g. Fornasa et al. (2016) for a recent example]. This corresponds to calculating the quantile function $\Delta_{\chi^2}(p)$ for only one degree of freedom.

Care has to be taken when using data-based covariances, such as the random patches and randomized flux, as the inverse of these covariances is biased (Kaufman 1967; Hartlap et al. 2007). To account for the effect of a finite number of realizations, the Gaussian likelihood in equation (17) should be replaced by a modified t-distribution (Sellentin & Heavens 2016). Alternatively, the effect of this bias on the uncertainties of inferred parameter can be approximately corrected (Hartlap et al. 2007; Taylor & Joachimi 2014). In light of the large systematic uncertainties in this analysis we opt for the latter approach when using the data based covariances.

5 RESULTS

5.1 Cross-correlation measurements

We present the measurement of the cross-correlation of *Fermi* gamma rays with CFHTLenS, RCSLenS and KiDS weak lensing data in Figs 6–8, respectively. The measurements for CFHTLenS and RCSLenS use a single redshift bin and the five energy bins described in Section 3.2. The measurements for KiDS use the same energy bins but are further divided into the five redshift bins given in Section 3.1.3.

Besides the cross-correlation of the gamma rays and shear due to gravitational lensing (denoted by black circles), we also show the cross-correlation between gamma rays and the B mode of the shear as red squares. The B mode of the shear is obtained by rotating the galaxy orientations by $45°$, which destroys the gravitational lensing signal. Any significant B-mode signal would be indicative of spurious systematics in the lensing data.

The χ_0^2 values of the measurements with respect to the hypothesis of a null signal, i.e. $\boldsymbol{\mu} = 0$, are listed in Table 2. The χ_0^2 values are consistent with a non-detection of a cross-correlation for all measurements. This finding is in agreement with the previous studies (Shirasaki et al. 2014, 2016) of cross-correlations between gamma rays and galaxy lensing. For a 3σ detection of the cross-correlation
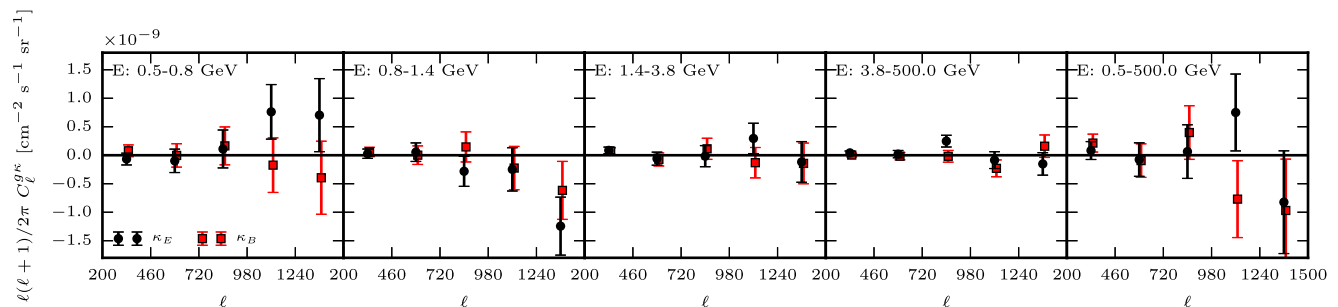
Figure 6. Measurement of the cross-spectrum $\hat{C}_\ell^{g\kappa}$ between *Fermi* gamma rays and weak lensing data from CFHTLenS for five energy bins for gamma-ray photons (black points). The cross-spectrum of the gamma rays and CFHTLenS B modes are depicted as red data points.
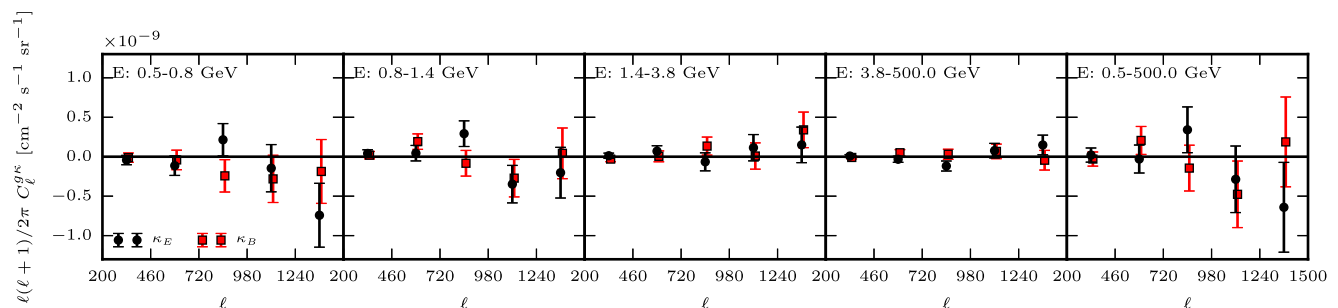
Figure 7. Measurement of the cross-spectrum $\hat{C}_\ell^{g\kappa}$ between *Fermi* gamma rays and weak lensing data from RCSLenS for five energy bins for gamma-ray photons (black points). The cross-spectrum of the gamma rays and RCSLenS B modes are depicted as red data points.

with astrophysical sources,[6] the error bars would have to shrink by a factor of 3 with respect to the current error bars for KiDS. This corresponds to an ∼4000 deg^2 survey with KiDS characteristics, comparable in size to the galaxy surveys used in Xia et al. (2015). This is further illustrated in Fig. 9, which shows the measurement for KiDS for the unbinned case in comparison with the expected correlation signal from astrophysical sources and annihilating dark matter for the HIGH scenario and $\langle\sigma_{\mathrm{ann}}v\rangle = 3 \times 10^{-26}\,\mathrm{cm}^3\,\mathrm{s}^{-1}$ for $m_{\mathrm{DM}} = 100\,\mathrm{GeV}$ and the $b\bar{b}$ channel. While these signals are not observable at current sensitivities, they are within reach of upcoming surveys, such as DES.[7]

The B-mode signal is consistent with zero for all measurements. We are thus confident that the measurement is not significantly contaminated by lensing systematics. At very small scales, lens-source clustering can cause a suppression of the lensing signal (van Uitert et al. 2011; Hoekstra et al. 2015). The angular scales we are probing in this analysis are, however, not affected by this.

5.2 Interpretation

We wish to exploit the measurements presented in the previous subsection to derive constraints on WIMP dark matter annihilation or decay. To derive the exclusion limits on the annihilation cross-section $\langle\sigma_{\mathrm{ann}}v\rangle$ and WIMP mass m_{DM}, and the decay rate Γ_{dec} and m_{DM}, we apply the formalism described in Section 4.3.

In Camera et al. (2015) it was shown that the spectral and tomographic information contained within the gamma-ray and lensing

data can improve the limits on $\langle\sigma_{\mathrm{ann}}v\rangle$ and Γ_{dec}. We show the effect of different combinations of spectral and tomographic binning for the case of KiDS and annihilations into $b\bar{b}$ pairs under the HIGH scenario in Fig. 10 and for dark matter decay in Fig. 11. For these limits we adopt the conservative assumption that all gamma rays are sourced by dark matter, i.e. no astrophysical contributions are included. There is a significant improvement of the limits when using four energy bins over a single energy bin, especially at high particle masses m_{DM}. This is due to the fact that the UGRB scales roughly as $E^{-2.3}$ (Ackermann et al. 2015c). The vast majority of the photons in the 0.5–500 GeV bin therefore come from low energies. However, the peak in the prompt gamma-ray emission induced by dark matter occurs at energy $\sim m_{\mathrm{DM}}/20$ (annihilating) or $\sim m_{\mathrm{DM}}/40$ (decaying) for $b\bar{b}$ and at higher energies for the other channels. Thus, for high m_{DM}, a single energy bin of 0.5–500 GeV largely increases the noise without significantly increasing the expected dark matter signal with respect to the 3.8–500 GeV bin.

The improvement due to tomographic binning is only marginal. Two factors contribute to this lack of improvement: first, in the case of no observed correlation signal – as is the case here – the differences in the redshift dependence of the astrophysical and dark matter sources do not come to bear because there is no signal to disentangle. Secondly, the lensing window functions are quite broad and thus insensitive to the featureless window function of the dark matter gamma-ray emissions, as depicted in Fig. 1. This is due to the cumulative nature of lensing on the one hand and the fact that photo-zs cause the true $n(z)$ to be broader than the redshift cuts we impose on the other hand. This is in contrast with spectral binning, which allows us to sharply probe the characteristic gamma-ray spectrum induced by dark matter. As shown in Fig. 3, annihilating dark matter shows a pronounced pion bump when annihilating into $b\bar{b}$ and a cutoff corresponding to the dark matter mass m_{DM}, while for decaying dark matter the cutoff appears at half the dark matter

---

[6] Cross-correlations between tracers of LSS and gamma rays have already been detected in Xia et al. (2015). A significant signal in the case of future weak lensing surveys is therefore a reasonable expectation.
[7] https://www.darkenergysurvey.org/
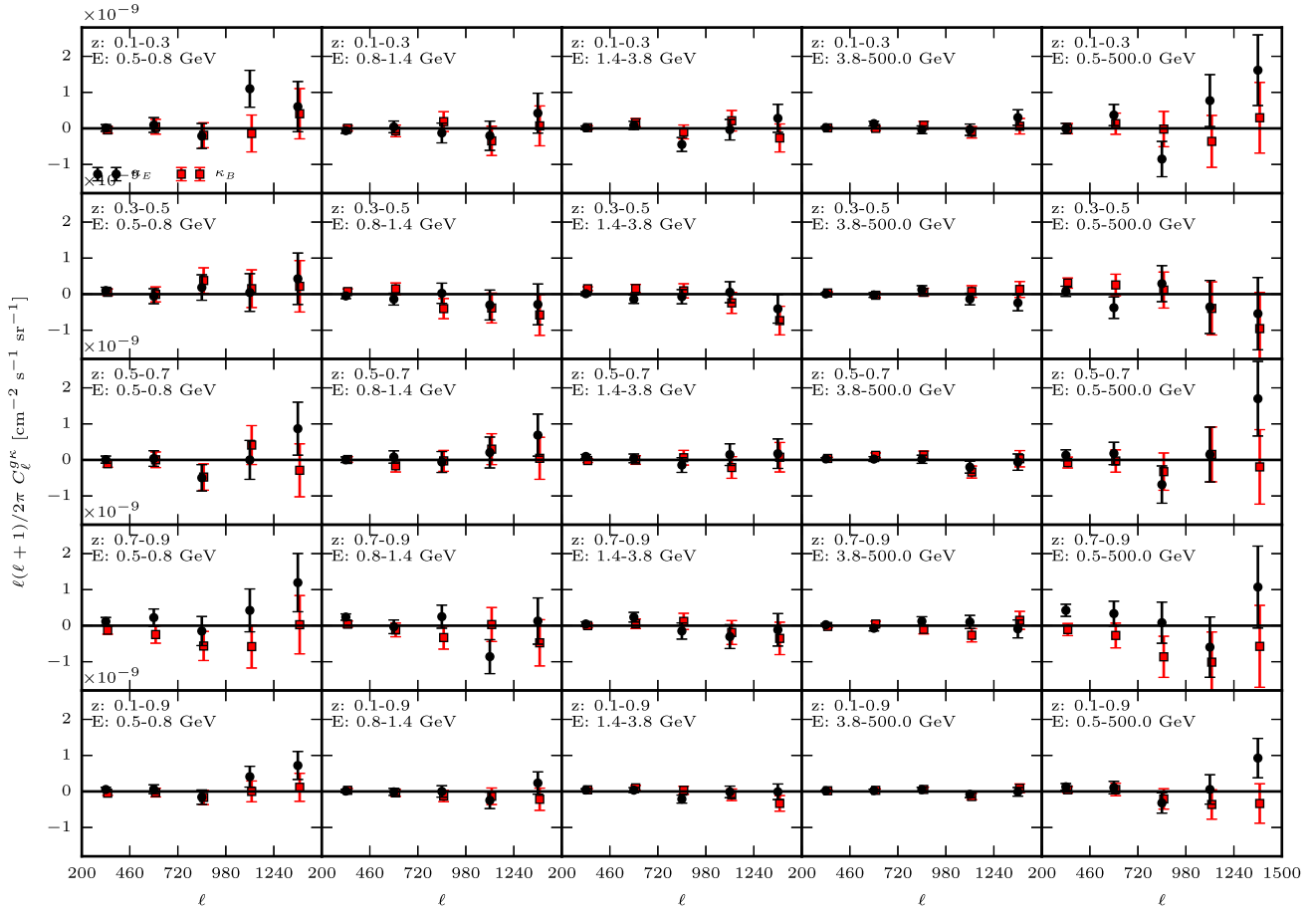
Figure 8. Measurement of the cross-spectrum $\hat{C}_\ell^{g\kappa}$ between *Fermi* gamma rays and weak lensing data from KiDS for five energy bins for gamma-ray photons and five redshift bins for KiDS galaxies (black points). The cross-spectrum of the gamma rays and KiDS B modes are depicted as red data points.

Table 2. χ_0^2 values with respect to the hypothesis of a null signal for the measurements of $\hat{C}_\ell^{g\kappa}$ shown in Figs 6–8. The number of degrees of freedom is the number of multipole bins, i.e. $\nu = 5$ for all measurements.

	$\chi_0^2\left(\hat{C}_\ell^{g\kappa}, \nu = 5\right)$				
Energy bin [GeV]	0.5–0.8	0.8–1.4	1.4–3.8	3.8–500.0	0.5–500.0
CFHTLenS	4.49	7.77	3.78	8.43	2.43
RCSLenS	6.06	6.75	2.39	6.47	3.19
KiDS $0.1 \leq z_B < 0.3$	5.96	1.85	6.53	6.89	8.47
KiDS $0.3 \leq z_B < 0.5$	1.84	1.94	2.75	3.42	2.77
KiDS $0.5 \leq z_B < 0.7$	3.27	1.89	4.02	2.56	5.57
KiDS $0.7 \leq z_B < 0.9$	4.82	11.42	4.98	2.88	8.76
KiDS $0.1 \leq z_B < 0.9$	7.16	1.81	5.42	3.05	6.55

mass. For this reason we refrain from a tomographic analysis for CFHTLenS and RCSLenS as we expect little to no improvements of the limits.

The limits can be further tightened by taking into account known astrophysical sources of gamma rays. This comes, however, at the expense of introducing new uncertainties in the modelling of said astrophysical sources. Going forward, we include the astrophysical sources to show the sensitivity reach of such analyses but also show the conservative limits derived under the assumption that all gamma rays are sourced by dark matter.

To account for the astrophysical sources, we subtract the combination of the three populations (blazars, mAGN and SFG) described in Section 2 from the observed cross-correlation signal. The dark matter limits are then obtained by proceeding as before but using

the residuals between the cross-correlation measurement and the astrophysical contribution. Since we assume no error on the astrophysical models, the limits obtained by including blazars, mAGN and SFG contributions should be considered as a sensitivity reach for a future situation where gamma-ray emission from these astrophysical sources will be perfectly understood.

The resulting 2σ exclusion limits on the dark matter annihilation cross-section $\langle \sigma_{\mathrm{ann}} v \rangle$ for the $b\bar{b}$, $\mu^-\mu^+$ and $\tau^-\tau^+$ channels are shown in Fig. 12. Finally, the combined exclusion limits for CFHTLenS, RCSLenS and KiDS are shown in Figs 13 and 14 for annihilating and decaying WIMP dark matter, respectively. The exclusion limits for annihilating dark matter should be compared to the thermal relic cross-section (Steigman et al. 2012), shown in grey. Under optimistic assumptions about the clustering of dark matter,
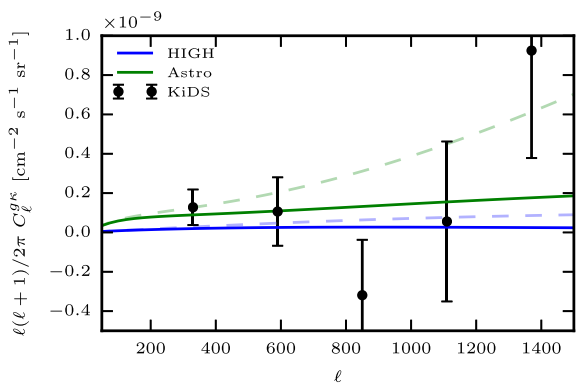
Figure 9. Measurement of the cross-spectrum $\hat{C}_\ell^{g\kappa}$ between *Fermi* gamma rays in the energy range 0.5–500 GeV and KiDS weak lensing data in the redshift range 0.1–0.9 (black data points), compared to the expected signal from the sum of astrophysical sources (solid green) and annihilating dark matter (solid blue). The astrophysical sources considered are blazars, mAGN and SFG. The annihilating dark matter model assumes the HIGH scenario, $m_{DM} = 100$ GeV, and $\langle\sigma_{ann}v\rangle = 3 \times 10^{-26}$ cm^{3}s^{-1}. The dashed lines show the same models but without correcting for the *Fermi* PSF.
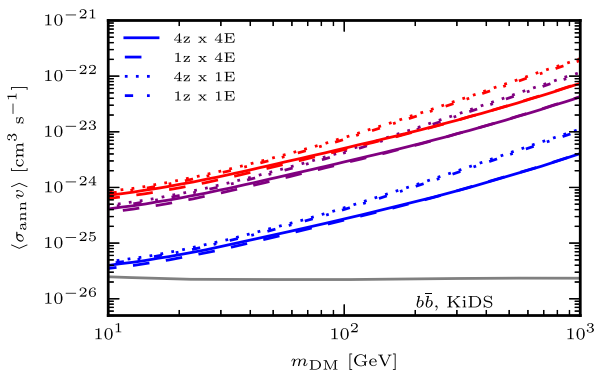
Figure 10. Exclusion limits on the annihilation cross-section $\langle\sigma_{ann}v\rangle$ and WIMP mass m_{DM} for the clustering scenarios HIGH (blue), MID (purple) and LOW (red) and for different binning strategies for the KiDS data. The lines correspond to 2σ upper limits on $\langle\sigma_{ann}v\rangle$ and m_{DM}, assuming a 100 per cent branching ratio into $b\bar{b}$. No binning in redshift or energy (1z x 1E) is denoted by dash–dotted lines. The case of binning in redshift but not energy (4z x 1E) is plotted as dotted lines, while binning in energy but not redshift (1z x 4E) is plotted as dashed lines. Finally, binning in both redshift and energy (4z x 4E) is shown as solid lines. The thermal relic cross-section, from Steigman, Dasgupta & Beacom (2012), is shown in grey.
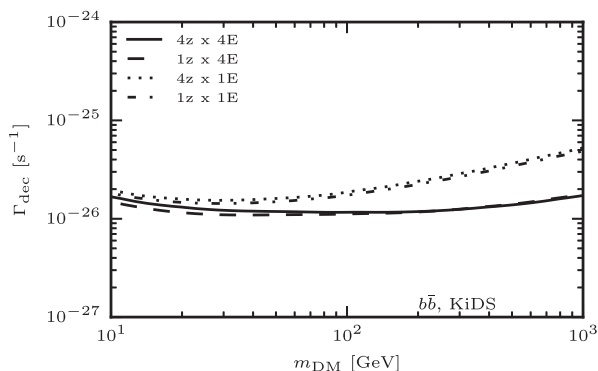
Figure 11. Exclusion limits on the decay rate Γ_{dec} and WIMP mass m_{DM} for the $b\bar{b}$ channel for different binning strategies for the KiDS data. The style of the lines is analogous to Fig. 10.

i.e. the HIGH model, and accounting for contributions from astrophysical sources (dashed blue line), we can exclude the thermal relic cross-section for masses $m_{DM} \lesssim 20$ GeV for the $b\bar{b}$ channel. In the case of annihilations or decays into muons or tau leptons, the exclusion limits change shape and become stronger for large dark matter masses, compared to the b channel. This is due to the fact that, for heavy dark matter candidates, inverse Compton scattering produces a significant amount of gamma-ray emission in the upper energy range probed by our measurement (Ando & Ishiwata 2016). If we make the conservative assumption that only dark matter contributes to the UGRB, i.e. we do not account for the astrophysical sources of gamma rays, the exclusion limits weaken slightly, as seen in the difference between the dashed and solid blue lines in Fig. 13. In this case the thermal relic cross-section can be excluded for $m_{DM} \lesssim 10$ GeV for the $b\bar{b}$ channel. These limits are consistent with those forecasted in Camera et al. (2015).

The exclusion limits when dark matter is assumed to be the only contributor to the UGRB are comparable to those derived from the energy spectrum of the UGRB in Ackermann et al. (2015a). However, when the contribution from astrophysical sources is accounted for, the limits in Ackermann et al. (2015a) improve by approximately one order of magnitude, while our limits see only modest improvements. This is due to the fact that we do not observe a cross-correlation signal. The constraining power therefore largely depends on the size of the error bars. The contribution from astrophysical sources is small compared to the size of our error bars, as shown in Fig. 9, explaining the modest gain in constraining power when including the astrophysical sources compared to probes that observe a signal. The exclusion limits obtained in Fornasa et al. (2016) from the measurement of the UGRB angular auto-power spectrum are stronger than the ones presented here. Those limits are dominated by the emission from dark matter subhaloes in the Milky Way, a component that is not considered in our analysis since it does not correlate with weak lensing. When restricting the analysis of the auto-spectrum in Fornasa et al. (2016) to only the extragalactic components, our cross-correlation analysis yields more stringent limits. The limits presented here are comparable to those of similar analyses of the cross-correlation between gamma rays and weak lensing (Shirasaki et al. 2014, 2016) but weaker than those derived from cross-correlations between gamma rays and galaxy surveys (Cuoco et al. 2015; Regis et al. 2015). The exclusion limits from all these extragalactic probes are somewhat weaker than those derived from dSphs (Ackermann et al. 2015b; Baring et al. 2016).

The weaker limits obtained when using KiDS data, compared to those obtained from RCSLenS data, can be traced to the high data point at small scales in the low energy bins. Restricting the analysis to the ℓ-range of 200 to 1240, i.e. removing the last data point, improves the limits derived from the KiDS to exceed those derived from RCSLenS, as one would expect from the covariances of the two measurements. To check whether the high data point is part of a trend that might become significant at even smaller scales, we extend the measurement to higher ℓ modes. Doing so reveals a high scatter of the data points around zero beyond $\ell \gtrsim 1500$, and no further excess of power at smaller scales. It should be noted that at these small scales, we are probing close to the pixel scale and are within the *Fermi* PSF, so the signal is expected to be consistent with zero there. Including astrophysical sources absorbs some of the effect of the high data point at small scales. The limits including astrophysical sources of gamma rays are thus closer than those assuming only dark matter as the source of gamma rays.
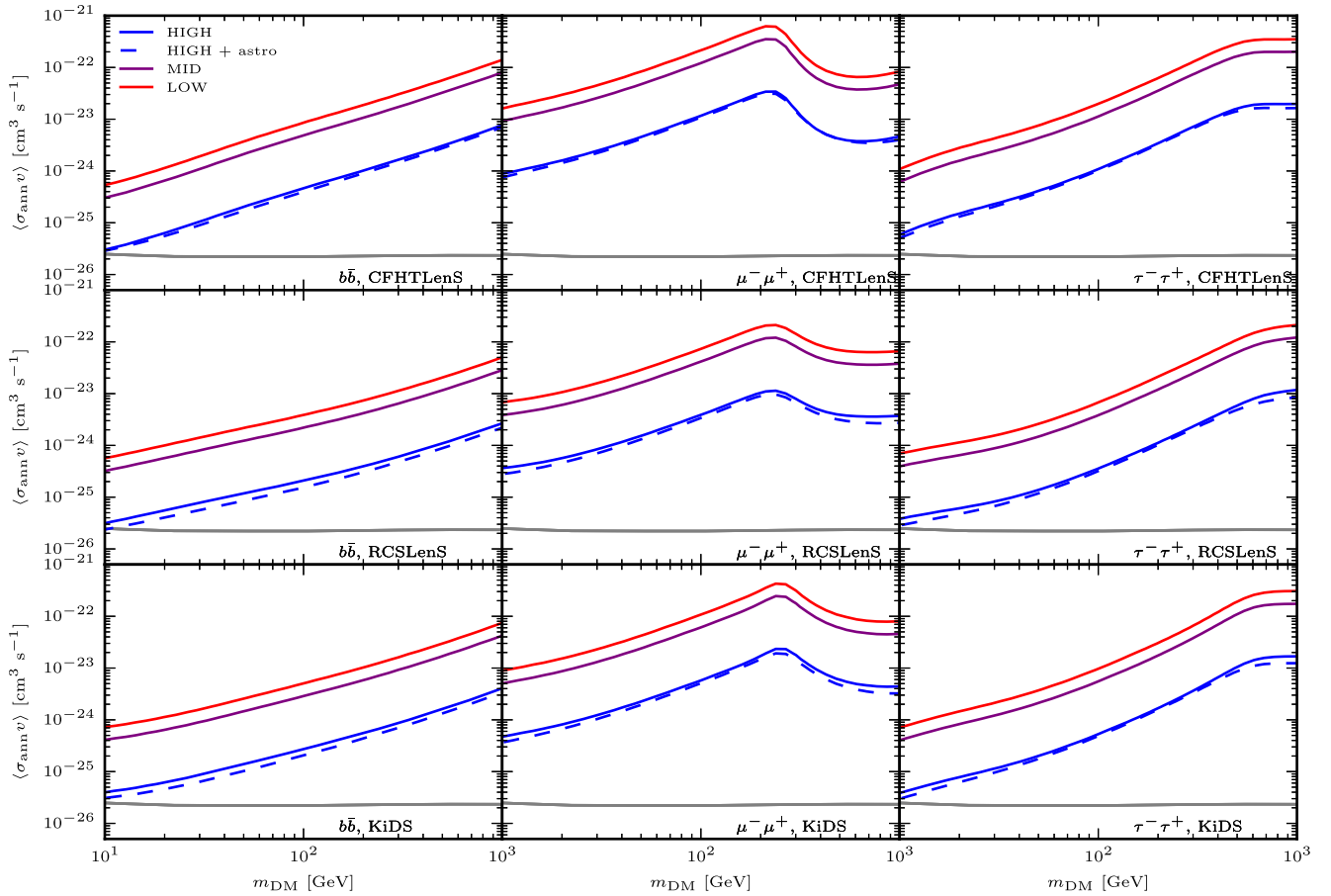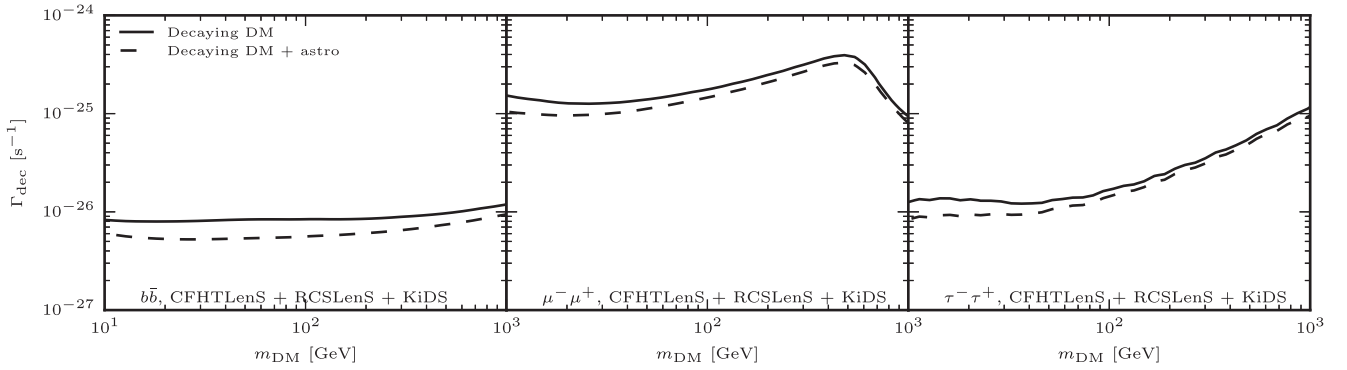
Figure 12. Exclusion limits on the annihilation cross-section $\langle \sigma_{ann} v \rangle$ and WIMP mass m_{DM} at 2σ significance for CFHTLenS, RCSLenS and KiDS and annihilation channels $b\bar{b}$, $\mu^-\mu^+$ and $\tau^-\tau^+$. CFHTLenS and RCSLenS use four energy bins while KiDS additionally makes use of four redshift bins. The exclusion limits are for the three clustering scenarios HIGH (blue), MID (purple) and LOW (red). The dashed blue line indicates the improvement of the limits for the HIGH scenario when including the astrophysical sources in the analysis.
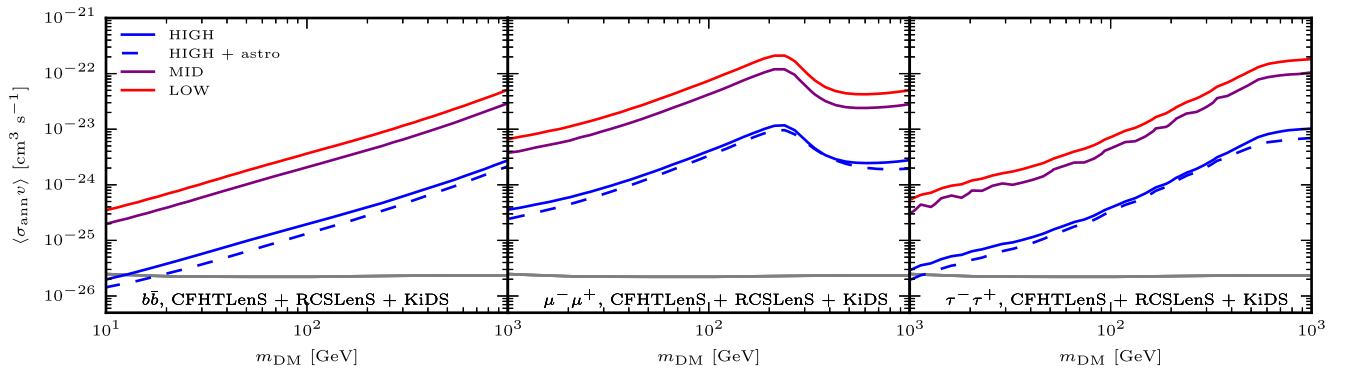
Figure 13. Exclusion limits on the annihilation cross-section $\langle \sigma_{ann} v \rangle$ and WIMP mass m_{DM} at 2σ significance for the combination of CFHTLenS, RCSLenS and KiDS. The style of the lines is the same as for Fig. 12.

6 CONCLUSION

We have measured the angular cross-power spectrum of *Fermi* gamma rays and weak gravitational lensing data from CFHTLenS, RCSLenS and KiDS. Combined together, the three surveys span a total area of more than 1000 deg². We made use of 8 years of Pass 8 *Fermi* data in the energy range 0.5–500 GeV which was divided further into four energy bins. For CFHTLenS and RCSLenS, the measurement was done for a single-redshift bin, while the KiDS data were further split into five redshift bins, making this the first

measurement of tomographic weak lensing cross-correlation. We find no evidence of a cross-correlation signal in the multipole range $200 \leq \ell < 1500$, consistent with previous studies and forecasts based on the expected signal and current error bars.

Using these measurements we constrain the WIMP dark matter annihilation cross-section $\langle \sigma_{ann} v \rangle$ and decay rate Γ_{dec} for WIMP masses between 10 GeV and 1 TeV. Assuming the HIGH model for small-scale clustering of dark matter and accounting for astrophysical sources, we are able to exclude the thermal annihilation

Figure 14. Exclusion limits on the decay rate Γ_{dec} and WIMP mass m_{DM} at 2σ significance for the combination of CFHTLenS, RCSLenS and KiDS (solid black). Including the astrophysical sources in the analysis results in the more stringent exclusion limits denoted by the black dashed line.

cross-section for WIMPs of masses up to ∼20 GeV for the $b\bar{b}$ channel. Not accounting for the astrophysical contribution weakens the limits only slightly, while the exclusion limits for the more conservative clustering models MID and LOW are a factor of ∼10 weaker. We find that tomography does not significantly improve the constraints. However, exploiting the spectral information of the gamma rays strengthens the limits by up to a factor of ∼3 at high masses.

The exclusion limits derived in this work are competitive with others derived from the UGBR, such as its intensity energy spectrum (Ackermann et al. 2015a), auto-power spectrum (Fornasa et al. 2016), cross-correlation with weak lensing (Shirasaki et al. 2014, 2016) or galaxy surveys (Regis et al. 2015; Cuoco et al. 2015). Exclusion limits derived from local probes, such as dSphs, are stronger, however (Ackermann et al. 2015b).

Future avenues to build upon this analysis include the use of upcoming large area lensing data sets, such as future KiDS data, DES, HSC,[8] LSST[9] and Euclid,[10] which will make it possible to detect a cross-correlation signal between gamma rays and gravitational lensing. The analysis would also benefit from extending the range of the gamma-ray energies covered, by making use of measurements from atmospheric Cherenkov telescopes, which are more sensitive to high-energy photons (Ripken et al. 2014).

Instead of treating the astrophysical contributions as a contamination to a dark matter signal, the measurements presented in this work could be used to investigate the astrophysical extragalactic gamma-ray populations that are thought to be responsible for the UGRB. We defer this to a future analysis.

ACKNOWLEDGEMENTS

[8] http://www.naoj.org/Projects/HSC/

[9] http://www.lsst.org/

[10] http://sci.esa.int/euclid/

REFERENCES

Acero F. et al., 2015, ApJS, 218, 23
Ackermann M. et al., 2012, ApJ, 755, 164
Ackermann M. et al., 2015a, J. Cosmol. Astropart. Phys., 9, 008
Ackermann M. et al., 2015b, Phys. Rev. Lett., 115, 231301
Ackermann M. et al., 2015c, ApJ, 799, 86
Ackermann M. et al., 2015d, ApJ, 810, 14
Ajello M. et al., 2015, ApJ, 800, L27
Anderson L. et al., 2014, MNRAS, 439, 83
Ando S., Ishiwata K., 2016, J. Cosmol. Astropart. Phys., 6, 045
Ando S., Komatsu E., 2006, Phys. Rev. D, 73, 023521
Ando S., Komatsu E., 2013, Phys. Rev. D, 87, 123539
Ando S., Benoit-Lévy A., Komatsu E., 2014, Phys. Rev. D, 90, 023514
Atwood W. B. et al., 2009, ApJ, 697, 1071
Baring M. G., Ghosh T., Queiroz F. S., Sinha K., 2016, Phys. Rev. D, 93, 103009
Bartelmann M., 2010, Class. Quant. Gravity, 27, 233001
Bertone G., Hooper D., Silk J., 2005, Phys. Rep., 405, 279
Bringmann T., 2009, New J. Phys., 11, 105027
Camera S., Fornasa M., Fornengo N., Regis M., 2013, ApJ, 771, L5
Camera S., Fornasa M., Fornengo N., Regis M., 2015, J. Cosmol. Astropart. Phys., 6, 29
Cembranos J. A. R., de La Cruz-Dombriz A., Dobado A., Lineros R. A., Maroto A. L., 2011, Phys. Rev. D, 83, 083507
Charles E. et al., 2016, Phys. Rep., 636, 1
Choi A. et al., 2016, MNRAS, 463, 3737
Cirelli M. et al., 2011, J. Cosmol. Astropart. Phys., 3, 051
Cooray A., Sheth R., 2002, Phys. Rep., 372, 1
Coupon J. et al., 2015, MNRAS, 449, 1352
Cuoco A., Xia J.-Q., Regis M., Branchini E., Fornengo N., Viel M., 2015, ApJS, 221, 29
de Jong J. T. A., Verdoes Kleijn G. A., Kuijken K. H., Valentijn E. A., 2013, Exp. Astron., 35, 25
Di Mauro M., Calore F., Donato F., Ajello M., Latronico L., 2014, ApJ, 780, 161
Erben T. et al., 2013, MNRAS, 433, 2545
Fenech Conti I., Herbonnet R., Hoekstra H., Merten J., Miller L., Viola M., 2016, MNRAS, preprint (arXiv:1606.05337)
Feng J. L., 2010, ARA&A, 48, 495
Feng C., Cooray A., Keating B., 2017, ApJ, 836, 127
Fornasa M., Sánchez-Conde M. A., 2015, Phys. Rep., 598, 1
Fornasa M. et al., 2013, MNRAS, 429, 1529
Fornasa M. et al., 2016, Phys. Rev. D, 94, 123005
Fornengo N., Regis M., 2014, Frontiers Phys., 2, 6
Fornengo N., Pieri L., Scopel S., 2004, Phys. Rev. D, 70, 103529
Fornengo N., Perotto L., Regis M., Camera S., 2015, ApJ, 802, L1
Franceschini A., Rodighiero G., Vaccari M., 2008, A&A, 487, 837
Gao L., Frenk C. S., Jenkins A., Springel V., White S. D. M., 2012, MNRAS, 419, 1721
Górski K. M., Hivon E., Banday A. J., Wandelt B. D., Hansen F. K., Reinecke M., Bartelmann M., 2005, ApJ, 622, 759
Gruppioni C. et al., 2013, MNRAS, 432, 23
Gunn J. E., Lee B. W., Lerche I., Schramm D. N., Steigman G., 1978, ApJ, 223, 1015
Harnois-Déraps J., van Waerbeke L., 2015, MNRAS, 450, 2857
Harnois-Déraps J. et al., 2016, MNRAS, 460, 434
Hartlap J., Simon P., Schneider P., 2007, A&A, 464, 399
Heymans C. et al., 2012, MNRAS, 427, 146

Hildebrandt H. et al., 2012, MNRAS, 421, 2355
Hildebrandt H. et al., 2016, MNRAS, 463, 635
Hildebrandt H. et al., 2017, MNRAS, 465, 1454
Hinshaw G. et al., 2013, ApJS, 208, 19
Hoekstra H., Herbonnet R., Muzzin A., Babul A., Mahdavi A., Viola M., Cacciato M., 2015, MNRAS, 449, 685
Hojjati A. et al., 2016, MNRAS, preprint (arXiv:1608.07581)
Hooper D., Profumo S., 2007, Phys. Rep., 453, 29
Ibarra A., Tran D., Weniger C., 2013, Int. J. Modern Phys. A, 28, 1330040
Jungman G., Kamionkowski M., Griest K., 1996, Phys. Rep., 267, 195
Kaufman G., 1967, Center for Operations Research and Econometrics, Catholic University of Louvain, Heverlee, Belgium, Report No. 6710
Kilbinger M. et al., 2013, MNRAS, 430, 2200
Kuijken K. et al., 2015, MNRAS, 454, 3500
Lee B. W., Weinberg S., 1977, Phys. Rev. Lett., 39, 165
Limber D. N., 1953, ApJ, 117, 134
Mantz A. B. et al., 2015, MNRAS, 446, 2205
Miller L. et al., 2013, MNRAS, 429, 2858
Moliné Á., Sánchez-Conde M. A., Palomares-Ruiz S., Prada F., 2017, MNRAS, 466, 4974
Navarro J. F., Frenk C. S., White S. D. M., 1997, ApJ, 490, 493
Planck Collaboration XIII, 2016, A&A, 594, A13
Prada F., Klypin A. A., Cuesta A. J., Betancort-Rijo J. E., Primack J., 2012, MNRAS, 423, 3018
Profumo S., Sigurdson K., Kamionkowski M., 2006, Phys. Rev. Lett., 97, 031301
Regis M., Xia J.-Q., Cuoco A., Branchini E., Fornengo N., Viel M., 2015, Phys. Rev. Lett., 114, 241301
Ripken J., Cuoco A., Zechlin H.-S., Conrad J., Horns D., 2014, J. Cosmol. Astropart. Phys., 1, 049
Ross A. J., Samushia L., Howlett C., Percival W. J., Burden A., Manera M., 2015, MNRAS, 449, 835
Sánchez-Conde M. A., Prada F., 2014, MNRAS, 442, 2271
Schmaltz M., Tucker-Smith D., 2005, Annu. Rev. Nucl. Part. Sci., 55, 229
Schneider P., van Waerbeke L., Kilbinger M., Mellier Y., 2002, A&A, 396, 1
Sellentin E., Heavens A. F., 2016, MNRAS, 456, L132
Sheth R. K., Tormen G., 1999, MNRAS, 308, 119
Shirasaki M., Horiuchi S., Yoshida N., 2014, Phys. Rev. D, 90, 063502
Shirasaki M., Horiuchi S., Yoshida N., 2015, Phys. Rev. D, 92, 123540
Shirasaki M., Macias O., Horiuchi S., Shirai S., Yoshida N., 2016, Phys. Rev. D, 94, 063522
Sjöstrand T., Mrenna S., Skands P., 2008, Comput. Phys. Commun., 178, 852
Steigman G., Dasgupta B., Beacom J. F., 2012, Phys. Rev. D, 86, 023506
Szapudi I., Prunet S., Pogosyan D., Szalay A. S., Bond J. R., 2001, ApJ, 548, L115
Taylor A., Joachimi B., 2014, MNRAS, 442, 2728
Taylor A., Joachimi B., Kitching T., 2013, MNRAS, 432, 1928
van Uitert E., Hoekstra H., Velander M., Gilbank D. G., Gladders M. D., Yee H. K. C., 2011, A&A, 534, A14
Xia J.-Q., Cuoco A., Branchini E., Viel M., 2015, ApJS, 217, 15

APPENDIX A: FOURIER-SPACE ESTIMATOR PERFORMANCE

To check the ability of the power spectrum estimator given by equation (12) to recover the true underlying power spectrum we test it on a suite of mock simulations. Specifically, we compare the auto-spectrum of the convergence with the estimated cross-spectrum between the convergence and the shear, which are expected to yield the same result. This is analogous to the cross-spectrum of the gamma rays and shear but easier to handle, as high-resolution simulation products for convergence and shear are readily available.

The simulation products we use are part of the Scinet LIght Cone Simulation suite (SLICS hereafter; Harnois-Déraps &
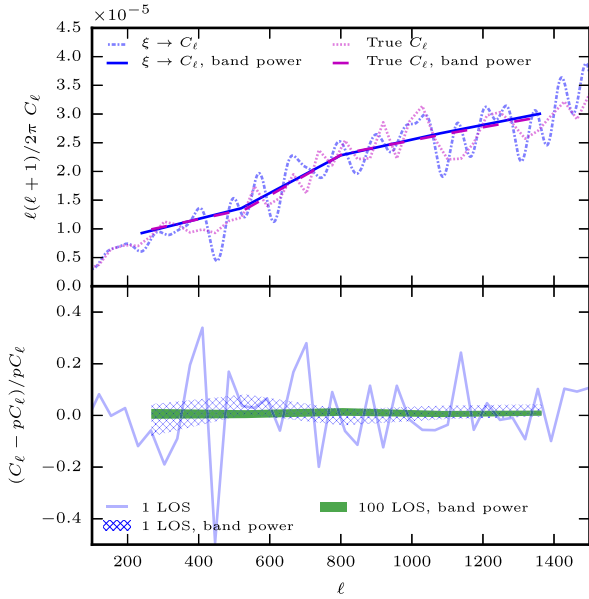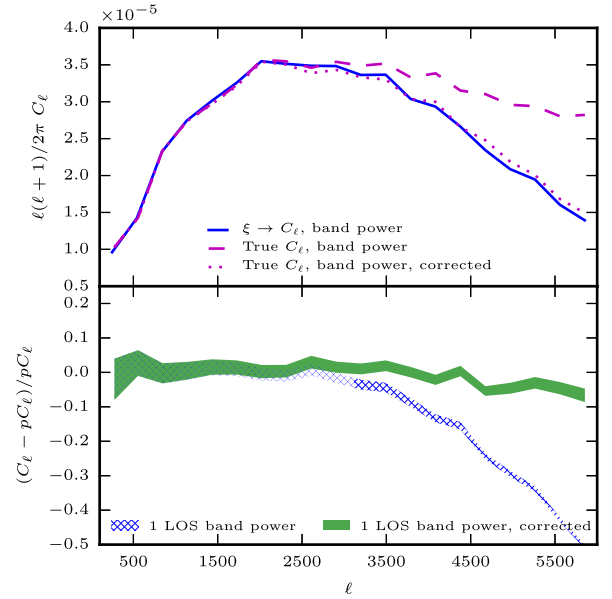
Figure A1. Top: power spectrum estimated using equation (12) (dash–dotted blue), band power (solid blue), true power spectrum (dotted magenta) and true band power (dashed magenta) for one line of sight. Bottom: difference between estimated and true power spectrum (light solid blue) for one line of sight, difference between the estimated and true band power for one line of sight (hashed blue) and 100 line of sights (solid green).

Figure A2. Top: band power spectrum estimated using equation (12) (solid blue), true band power (dashed magenta), and true band power corrected for the effect of finite $\vartheta_{\min}$ in equation (A1)(dotted magenta). Bottom: difference between estimated band power and true band power (solid green) and corrected for finite $\vartheta_{\min}$ (hashed blue).

van Waerbeke 2015), which consist of 930 realizations of lensing data over 10×10 deg^2 patches in a *WMAP*9+SN+BAO cosmology ({Ω_M, Ω_Λ, Ω_b, σ_8, h, n_s} = {0.2905, 0.7095, 0.0473, 0.826, 0.6898, 0.969}). The convergence and two shear components are constructed by ray-tracing up to 18 density planes between redshift zero and 3, and finally mapped on to 7745^2 pixels (see the SLICS reference for details about how this is implemented numerically). For our particular setup, we use the maps constructed while assuming that the galaxy sources are all placed at redshift 0.582. This is of course not representative of the real galaxy distribution of the data, but closely matches the mean of the distribution, which is sufficient for the purpose of calibration.

For the purpose of the verification of our estimator in equation (12), we use a subset of 100 realizations. The convergence and shear maps are cropped to 7700^2 pixels and then down-sampled by a factor of 10 to closer resemble the pixel size encountered in the gamma-ray analysis.

We measure the tangential shear correlation function between the convergence and shear maps using the same binning scheme as the gamma-ray cross-correlation measurement, i.e. 300 linearly spaced bins between 1 and 301 arcmin. The power spectrum estimated using equation (12) is then expected to agree with the auto-power spectrum of the convergence map $C_\ell^{\kappa\kappa}$. The power spectra measured on the simulations are shown in Fig. A1. For the scales of interest in this work the estimator recovers the power spectrum to within 5 per cent on individual line of sights, which is within the error on the mean per ℓ-bin of the true power spectrum. The agreement is within ∼1 per cent for 100 line of sights, which is within the error on the mean of the 100 true power spectra, showing that the fluctuations seen on individual line-of-sight average out.

One caveat is that the range of integration in equation (12) is formally from 0 to infinite angular separation. By restricting the integration to some finite range $\vartheta_{\min}$ to $\vartheta_{\max}$, the resulting power spectrum estimate can become biased.

To estimate the effect of restricting the angular range of the two-point correlation function on the power spectrum estimate we produce a high-resolution measurement of the convergence power spectrum $C_\ell^{\kappa\kappa}$. Using the relation in equation (2) between the power spectrum $C_\ell^{\kappa\kappa}$ and the tangential shear correlation function $\xi^{\kappa\gamma_t}(\vartheta)$, we compute a theory estimate $\xi_{th}^{\kappa\gamma_t}(\vartheta)$ from the measured high-resolution convergence power spectrum. Alternatively, we could also have used an analytical model for the power spectrum or correlation function. However, in order to make the comparison between the different power spectrum estimates as direct as possible, we chose to minimize the amount of external information.

Finally, to estimate the effect of restricting the range of integration we compute the correction terms

$$C_\ell^{\vartheta_{\min}} = 2\pi \int_0^{\vartheta_{\min}} d\vartheta' \, \vartheta' J_2(\ell\vartheta') \xi_{th}^{\kappa\gamma_t}(\vartheta') \tag{A1}$$

and

$$C_\ell^{\vartheta_{\max}} = 2\pi \int_{\vartheta_{\max}}^{\infty} d\vartheta' \, \vartheta' J_2(\ell\vartheta') \xi_{th}^{\kappa\gamma_t}(\vartheta'). \tag{A2}$$

The effect of the minimum angular separation $\vartheta_{\min}$ is a suppression of power at small scales, restricting the range of scales where the power spectrum estimate is unbiased. However, by forward modelling, i.e. accounting for the effect of the minimum angular separation when comparing the measurements to models, the effective range can be increased significantly. This can be seen in Fig. A2, where accounting for $C_\ell^{\vartheta_{\min}}$ increases the range of validity from $\ell \sim 2000$ to $\ell \sim 6000$. On the scales considered in the main body of this work ($\ell \leq 1500$) the effect of a finite ϑ is negligible and no forward modelling of this effect was conducted.
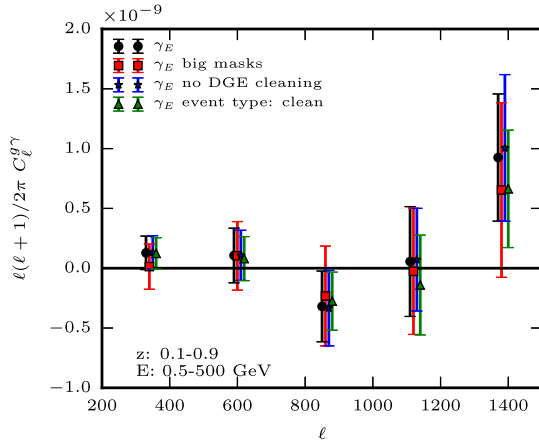
Figure A3. Measurement of the cross-spectrum $\hat{C}_\ell^{g\kappa}$ between *Fermi* gamma rays in the energy range 0.5–500 GeV and KiDS weak lensing data in the redshift range 0.1–0.9 for different gamma-ray data preparation choices: fiducial, as described in Section 3.2 (black points); using two-degree radius circular masks for all point sources (red squares); no cleaning of the DGE (blue stars); and using the `clean` event selection (green triangles).

A finite maximum angular separation ϑ_{max} does not lead to a systematic bias in the power spectrum estimation like the effect of ϑ_{min}. The oscillatory nature of the estimated power spectrum requires the use of band power, however. The width of the bins results in an effective lower limit on the scales that can be estimated. For fixed ϑ', the Bessel function in equation (12) oscillates with period of $\sim \frac{2\pi}{\vartheta'}$. The shortest period that can be probed is therefore $\sim \frac{2\pi}{\vartheta'_{max}}$. Requiring two to three periods per ℓ-bin, the minimum reliable bin width for a maximum angular separation of $\vartheta_{max} = 301$ arcmin is therefore $\Delta_\ell \sim 200$. The bin width chosen in this work is $\Delta_\ell = 260$ and can thus be assumed to yield a reliable estimate of the power spectrum.

This paper has been typeset from a TEX/LATEX file prepared by the author.